On the Nature and Extent of Optically-Thin Marine Low-Clouds

L. V. Leahy*, R. Wood, and R. J. Charlson

Department of Atmospheric Sciences, University of Washington, Seattle, Washington, USA

C. A. Hostetler, R. R. Rogers

NASA Langley Research Center, Hampton, VA

M. A. Vaughan, D. M. Winker

NASA Langley Research Center, Hampton, VA

Submission for publication to *Journal of Geophysical Research:*

Corresponding Author*: Louise Leahy

University of Washington

Department of Atmospheric Sciences

Box 351640

Seattle, WA 98195-1640 USA

Tel: (206) 543 4250

Fax: (206) 543 0308

Email:lleahy@atmos.washington.edu

Abstract

Macrophysical properties of optically-thin marine low-clouds over the non-polar oceans (60°S-60°N) are measured using two years of full-resolution nighttime data from the Cloud-Aerosol Lidar with Orthogonal Polarization (CALIOP). Optically-thin clouds, defined as the subset of marine low-clouds that do not fully attenuate the lidar signal, comprise almost half of the low-clouds over the marine domain. Regionally, the fraction of low-clouds that are optically-thin ($f_{\text{thin,cld}}$) exhibits a strong inverse relationship with the mean low-cloud cover, with maxima in the tropical trades ($f_{\text{thin,cld}} > 0.8$) and minima in regions of persistent marine stratocumulus ($f_{\text{thin,cld}} < 0.3$). Domain-wide, a power law fit describes the cloud length distribution of low-clouds, with exponent $\beta = 2.03 \pm 0.06$ (± 95% confidence interval). The mean fraction of each cloud that is optically-thin decreases from close to unity for clouds smaller than 2 km, to less than 0.3 for clouds larger than 30 km. This relationship is found to be independent of region, and geographical variations in the cloud length distribution explain three-quarters of the variance in $f_{\text{thin,cld}}$. Comparing collocated trade wind cumulus observations from CALIOP and the airborne High Spectral Resolution Lidar (HSRL) reveals that clouds with lengths smaller than are resolvable with CALIOP contribute approximately half of the low-clouds in the region sampled. A bounded cascade model is constructed to match the observations from the trades. The model shows that the observed optically-thin cloud behavior is consistent with a power law scaling of cloud optical depth, and that most optically-thin clouds only partially fill the CALIOP footprint.

1.0 Introduction

The planetary albedo is a critical determinant of the Earth's temperature. It is a complex quantity determined by the reflection of sunlight by the Earth's surface and atmosphere. Because of the importance of albedo to Earth's temperature and climate, it is imperative that its controlling factors be understood and be adequately quantified. Without clouds, the planetary albedo would be about 0.15, due to the low reflectance of the Earth's surface (most of which is ocean). Highly reflective surfaces, such as those characteristic of polar regions and unvegetated deserts, are notable exceptions but cover a small part of the planet and do not contribute strongly to the average surface albedo. However, the average albedo of the Earth (~0.3) is roughly doubled by the presence of clouds [*Harrison et al.*, 1990], and low-clouds are the dominant type by contribution to albedo [*Hartmann et al.*, 1992].

Among albedo-influencing components of the Earth system, clouds are unique in both their extreme transience and in the remarkable range of sizes and forms that they assume. Although we have a reasonably accurate assessment of the global impact of clouds on the planetary albedo, our understanding of how clouds of different sizes and types contribute to the albedo remains rather poor. Whereas it is known that low-clouds are the dominant contributor to the albedo globally [*Hartmann et al.*, 1992], it is uncertain what the relative contributions of the different low-cloud types (cumulus, stratocumulus, stratus) are to the overall albedo of low-clouds.

Moist convection over the oceans has a varied morphology. Marine low-clouds range from expansive stratocumulus decks stretching hundreds of kilometers, to small trade wind cumulus a few tens to hundreds of meters in extent [*Hozumi et al.*, 1982; *Wood and Field*, 2011]. We are currently unable to quantify how different low-cloud systems

69 distribute condensate horizontally and vertically to determine their albedo. This is partly
70 because we do not fully understand how albedo scales with cloud cover, as the latter is
71 frequently difficult to measure with the moderate-resolution (~1 km) passive sensors used to
72 generate our cloud cover climatologies [*Zhao and Di Girolamo*, 2006]. We still do not have
73 proven measures of cloud condensate amounts, particularly for broken and thin cloud fields
74 [*Turner et al.*, 2007]. Many questions are therefore still unanswered. For example, per unit
75 of cloud cover, are trade cumulus clouds optically thinner than stratocumulus? What
76 fraction of low-clouds are optically-thin and how are these optically-thin clouds partitioned
77 by cloud length and type? What resolution do our passive sensors need to have in order to
78 accurately determine cloud cover?
79 Satellite data show that the albedo of extensive marine low-clouds is quite low
80 [*Bender et al.*, 2011], and that their optical thickness is highly variable (e.g., *Rossow et al.*
81 [2002]). It is reasonable to infer that a significant fraction of them must be optically-thin.
82 These optically-thin clouds are not currently well resolved observationally, but are globally
83 pervasive and potentially important for climate studies [*Turner et al.*, 2007; *Zuidema et al.*,
84 2012]. For this work, we define operationally, an optically-thin cloud as a cloud that does
85 not fully attenuate a lidar backscatter signal; which corresponds to a maximum cloud optical
86 depth (τ_{cld}) ~3. Analysis of Moderate Resolution Imaging Spectroradiometer (MODIS)
87 Level 3 liquid water τ_{cld} over ocean, suggests clouds with τ_{cld} less than 3 comprise ~30% of
88 marine low-clouds, at MODIS 1 km resolution, and contribute perhaps 15% of their albedo
89 (Fig. 1), when analyzed in terms of optical depth increments. But since many of these
90 clouds are smaller than the resolution of the MODIS pixels (e.g., *Zhao and Di Girolamo*,
91 [2007]), it is important to appreciate that these estimates are likely to be a function of sensor
92 resolution. How does the picture change when clouds are viewed with an active sensor with

93 a much smaller footprint size? Indeed, does the use of metrics such as cloud cover even
94 make sense when a significant fraction of the clouds have very low optical thicknesses?
95 Optically-thin and broken clouds are not only important because of their
96 contribution to the planetary albedo, but because aerosol retrievals are problematic where
97 clear regions are in close proximity to clouds, and contamination of clear pixels by sub-
98 pixel scale optically-thin clouds is common (e.g., *Zhang and Reid* [2005], *Charlson et al.*
99 [2007], *Koren et al.* [2007]). A trade wind cumulus study reported that a third of MODIS
100 pixels diagnosed by the cloud mask as being clear actually contained sub-pixel scale cloud
101 [*Zhao and Di Girolamo,* 2006]. Over the global ice-free oceans, 50% of marine low-clouds
102 are separated from each other by less than 5 km [*Várnai and Marshak,* 2011], suggesting
103 that a high fraction of clear sky over ocean is in close proximity to cloud. Other recent
104 studies of the clear-cloud transition region using both in situ [*Twohy et al.,* 2009] and
105 remote sensing measurements [*Su et al.,* 2008; *Tackett and Di Girolamo,* 2009; *Redemann*
106 *et al.,* 2009] suggest that aerosol properties in the vicinity of clouds are different to those 2-
107 5km from the cloud. Some of this difference may be attributed to aerosol hygroscopic
108 growth in the high relative humidity air surrounding cloud, but the relative magnitudes of
109 cloud contamination and aerosol hygroscopic growth effects on retrieved aerosol properties
110 is not known. Observations show that enhancement of near-cloud reflectances due to
111 undetected or unresolved cloud contamination of clear pixels leads to passive sensor aerosol
112 optical depth retrieval overestimates of 10-20% [*Zhang and Reid,* 2005].
113 Although passive sensors provide excellent coverage, it is fundamentally
114 challenging to identify which atmospheric constituents are producing the measured top of
115 atmosphere (TOA) signals, and at what altitudes they reside. Spaceborne lidar provides a
116 metric of the TOA reflectance, integrated over the specified layers of interest, and offers a

117 closer link to the atmospheric constituent producing that signal. A frequency distribution of
118 such a metric, integrated attenuated backscatter (IABS), derived from high-resolution (90 m
119 telescope footprint) Cloud-Aerosol Lidar with Orthogonal Polarization (CALIOP) is
120 presented in Fig. 2. A bimodal distribution of IABS is observed with modes representing
121 clear and cloudy atmospheric states as indicated (Fig. 2a). The non-zero minimum between
122 clear and cloudy states, which exemplifies the fundamental challenge in separating clouds
123 from clear sky, has been termed the "continuum" region [*Charlson et al.,* 2007]. With
124 detailed classification with CALIOP's full-resolution cloud clearing algorithm [*Vaughan et*
125 *al.,* 2009]), spaceborne lidar is able to inform us that this "continuum", or clear-cloud
126 transition region, is populated almost exclusively with clouds (Fig. 2b). These clouds must,
127 by their virtue of having low visible reflectance, be optically-thin. IABS can be small
128 either because the cloud is optically-thin or because the laser was attenuated fully some
129 distance into an optically-thick cloud. The latter case is manifest in Fig. 2b as the smaller
130 values of IABS categorized as optically-thick cloud. A frequency distribution alone cannot
131 inform us of their spatial structure, but previous work suggests a prevalence of detraining
132 cloud elements, dissipating, or nascent clouds in marine low-cloud systems [*Koren et al.*,
133 2009]. However, the CALIOP data are showing us that optically-thin clouds are not only
134 limited to the "continuum" region, but contribute to TOA reflectance throughout the entire
135 low-end of the cloud IABS distribution (Fig. 2b). Indeed, over non-polar oceans, we find
136 that almost half of the marine low-clouds are optically-thin.

137 Despite the apparent prevalence of optically-thin clouds, very little is currently
138 known about their macrophysical properties (spatial distribution, length, vertical
139 distribution, geometric depth) on a global scale. This study aims to provide insight into
140 these properties, and thereby provide new information on a poorly characterized and

141 understood subset of marine low-clouds. Large scale models tend to overestimate the
142 frequency of optically-thick low-clouds and underestimate the frequency of optically-thin
143 low-clouds [*Kay et al.*, 2012]. At the low-end of the optical depth distribution, model
144 frequencies are close to an order of magnitude too low compared to passive remote sensing
145 satellite observations [*Kay et al.*, 2012]. However, it is important to appreciate that there
146 are major differences between observational datasets, making assessment of model
147 representation of optically-thin low-clouds difficult.

148 The primary dataset employed for this study is the CALIOP full-resolution cloud
149 mask (60 m vertical, and 335 m horizontal resolution) at 1064 nm. In addition to providing
150 new near-global observations of the macrophysical properties of optically-thin marine low-
151 clouds, we also investigate possible sensor-resolution detection issues by comparing
152 CALIOP with data from NASA's airborne High Spectral Resolution Lidar (HSRL). The
153 ensuing sections of this manuscript are ordered as follows. Dataset description and analysis
154 methodology are detailed in Section 2. Results are presented in Sections 3. A discussion of
155 the implications is augmented and informed by the use of a simple fractal model in Section
156 4. Our findings are summarized in Section 5.

157
158

2.0 Dataset Description and Analysis Method

2.1 CALIOP Dataset

Two years (September 2006-August 2008) of vertically-resolved cloud data from the full-resolution CALIOP Vertical Feature Mask (VFM) Version 3.01 [*Vaughan et al.*, 2009] over the non-polar oceans (±60° latitude) are used in this study. The VFM provides vertically-resolved cloud and aerosol layer information generated by the CALIOP multi-resolution layer identification and scene classification algorithms. Full-resolution layer information is obtained from the high-resolution cloud clearing tool within the layer detection algorithm. In the lowest 4 km of the atmosphere the 1064 nm channel (60 m vertical resolution) is used for full-resolution cloud-layer identification. This wavelength is less sensitive to aerosol than the 532 nm channel and thus improves cloud-aerosol discrimination. A detailed mission overview and comprehensive instrument details are presented by *Winker et al.* [2009], and *Hunt et al.* [2009], respectively. CALIOP has high sensitivity at low cloud optical depths: nighttime minimum detectable particulate extinction at 1064 nm is 0.165 km^{-1} for layers greater than 180 m in depth, equivalent to τ_{cld} greater than 0.03, and is 1.65 km^{-1} for layers less than 180 m (minimum 60 m), equivalent to τ_{cld} greater than 0.1 (Chepfer, H., G. Cesana, D. Winker, B. Getzewich, and M. Vaughan, Comparison of two different cloud climatologies derived from CALIOP-Level 1 observations: the CALIPSO-ST and the CALIPSO-GOCCP, submitted to *Journal of Atmospheric and Oceanic Technology*, 2012). CALIOP provides near-global (± 82° latitude), vertically-resolved, atmosphere-only backscatter data, with no contamination from surface return or 3-D radiation/cloud adjacency effects, unlike radiances measured from passive sensors [*Wen et al.*, 2007; *Várnai and Marshak*, 2009]. However, sampling is sparse. The lidar return signal is limited to a 90 m diameter receiver footprint, so no off-

183 track atmospheric information can be provided. In addition, consecutive laser footprints are
184 not contiguous; horizontal separation between each footprint is 335 m and consecutive
185 nighttime (and daytime) orbits are ~2,600 km apart at the Equator, requiring a temporally
186 extensive dataset for representative sampling.

187 Our focus is optically-thin marine low-clouds. In this study, a low-cloud is defined
188 as having a cloud top height (CTH) less than or equal to 3 km. A high cloud is any cloud
189 higher than this. We define an optically-thin cloud as a cloud detected at full-resolution that
190 does not fully attenuate the lidar signal (i.e., one for which the ocean surface was also
191 detected in the same profile), corresponding to τ_{cld} less than or equal to 3. Optically-thick
192 clouds are all other low-cloud not classified as optically-thin. We screen the data for both
193 high clouds, and incidences of low-clouds where more than one cloud-layer is detected, the
194 latter representing a small fraction of the marine low-cloud data, 0.06 on average. To
195 ensure the highest fidelity in our results, we use only nighttime data for optimal detection of
196 optically-thin clouds; the solar background signal degrades the daytime signal-to-noise ratio
197 (SNR) [*Hunt et al.*, 2009]. The daytime minimum detectable particulate extinction at 1064
198 nm is 0.28 km^{-1}, equivalent to τ_{cld} greater than 0.05 for layers greater than 180 m in depth,
199 and is 2.8 km^{-1} for layers less than 180 m in depth (minimum 60 m), equivalent to τ_{cld}
200 greater than 0.17. Inspection of daytime IABS distributions does not reveal large
201 differences between daytime and nighttime data, but it is not possible to separate real
202 diurnal differences from potential differences in detectability and other noise-related
203 artifacts. We note that some aerosol layers (e.g., Saharan dust) may be dense enough to
204 be misclassifiied as cloud at full-resolution, however, this occurs mostly over land and we
205 assume the effects over ocean to be negligible. In this work a profile is defined as a column
206 of vertically-resolved VFM clear or cloud classifications derived from a single lidar pulse.

We further define a cloudy profile as a full-resolution profile with one or more 60 m vertically adjacent cloud-layers. In summary, our primary dataset is comprised of clear profiles and single-layer cloudy profiles with CTH less than or equal to 3 km detected at full-resolution at night over non-polar oceans.

To provide an example of optically-thin clouds and spatial context, we present collocated Wide Field Camera (WFC) band-averaged radiance (620 – 670 nm) for a 10 km orbit segment at 125 m horizontal resolution, and CALIOP full-resolution Level 1 daytime IABS at 532 nm integrated from 0 to 20 km, for a broken cloud field in the northwest subtropical Atlantic (Fig. 3). Along with CALIOP, the WFC is part of the Cloud Aerosol Lidar with Integrated Pathfinder Satellite Observation (CALIPSO) satellite's payload. The WFC context (Fig. 3a) suggests that some detected optically-thin cloud profiles are cloud edges that partially fill the lidar field of view. We explore this issue further in Section 4. In general, peaks and troughs observed in both the radiance and IABS data track each other remarkably well (Fig. 3b). Optically-thick cloud profiles (fully attenuated profiles) tend to be associated with stronger visible radiances. However, radiances associated with optically-thick clouds at ~6 km along the orbit segment are similar to some of the radiances for optically-thin cloud profiles elsewhere. The lack of a complete correspondence between radiance and IABS is indicative of the different nature of the lidar backscatter signal and the visible reflectance. Multiple scattering affects the signals in different ways. In addition, it is likely that beam filling in this broken cloud field affects visible radiance and lidar signals differently. The clear evidence in this example for small and often optically-thin cloud elements on the scale of the lidar footprint compels us to understand how optically-thin clouds are related to cloud horizontal scales globally and regionally.

2.2 HSRL Dataset

In addition to a near-global examination of CALIOP's view of optically-thin marine low-clouds, we also compare collocated CALIOP cloud fractions and cloud lengths with those estimated using the airborne NASA LaRC High Spectral Resolution Lidar (HSRL) [*Hair et al.*, 2008]. Although HSRL is typically employed for aerosol studies and/or instrument validation e.g. *Kacenelenbogen et al.* [2011], *Rogers et al.* [2011], for this work we utilize HSRL altitudes of surface and cloud top. Cloud data for the comparison are drawn from four daytime and four nighttime spatially and temporally matched HSRL underflights of the CALIOP orbit track over the tropical and subtropical western Atlantic (Table 1), and we include only data for flight segments with aircraft altitude greater than 8 km. HSRL cloud-screening is based upon a wavelet transform technique [*Su et al.*, 2008]. HSRL and CALIOP do not have the same footprint dimensions due to different sampling configurations. The HSRL sample area is composed of 60 m along-track averages of contiguous 8 m single-shot footprints, yielding a sample area 8 m x 60 m in the in the across-track and along-track directions, respectively. The 60 m along-track dimension results from 2 Hz sampling at aircraft ground-speed of 120 m s^{-1} (mean value for data analyzed herein). However, CALIOP 90 m diameter footprints are horizontally separated by 335 m in the along-track direction. Note, from hereon in, we refer to an instrument footprint, pixel size or sample area as a field of view (FOV), for clarity of notation. HSRL data have 30 m vertical resolution. We identify cloudy HSRL profiles as those with CTH less than or equal to 3 km. We use the HSRL surface altitude parameter to determine whether a surface return was detected and thereby discriminate between low and high optical depth clouds, i.e., whether or not the signal was fully-attenuated by the cloud before reaching the surface. For the ocean data used, we expect the surface altitude for a cloud

255 profile to be ~ 0 m if the signal is not fully attenuated. However, the surface altitude
256 parameter is not fully developed (HSRL Data Summary, unpublished material, 2009) and
257 departs somewhat from 0 m, even for cloud-free profiles over the ocean. Therefore, we
258 define a cloud profile with surface altitude less than or equal to 85 m as optically-thin. The
259 upper limit of 85 m is the mean surface altitude plus three standard deviations observed for
260 cloud-free HSRL profiles over the ocean. For the HSRL-CALIOP comparisons, we include
261 only HSRL and CALIOP data that achieve temporal coincidence within ± 15 minutes. Both
262 datasets are high-cloud-screened using the CALIPSO VFM described in Section 2.1
263
264 2.3 Analysis Methods
265 After screening for high-cloud, CALIOP full-resolution data are binned into 5° x 5°
266 latitude-longitude gridboxes. Gridding the data allows us to examine the geographical
267 variations of the various cloud features examined. We define a transect as being the portion
268 of ground track for each CALIPSO orbit within a gridbox. Separate analysis methods are
269 applied to these binned data to produce cloud cover statistics, and cloud length distributions.
270
271 2.3.1 Cloud Cover Analysis Method
272 Monthly cloud cover values calculated from counts of full-resolution clear profiles
273 and low-cloud profiles within a gridbox (Table 2) are averaged to produce two-year mean
274 low-cloud cover values for each gridbox. Domain-wide cloud cover is the mean of all
275 gridbox values.
276 Minima in high-cloud-screened CALIOP profile counts (Fig. 4a) exhibit a similar
277 pattern to ISCCP – D2 cloud amount maxima for mid plus high clouds (available from
278 http://isccp.giss.nasa.gov/products/browsed2.html). ISCCP annual mean data (not shown)
279 indicate maximum high cloud amounts in the western equatorial Pacific and northern Indian

Ocean (amounts > 40%), and mid-level cloud amount maxima (30-40%) in the Northern and Southern Hemisphere storm-track regions.

2.3.2 Cloud Length Distribution Method

Cloud length is calculated for individual cloud entities. We define a cloud entity as a series of consecutive marine low-cloud profiles, bounded on each end by a clear profile. The cloud length data are binned into logarithmically spaced size bins, with the lower size limit set by instrument resolution, and the upper limit defined by the sampling method discussed below. An additional criterion is applied to the size distribution data that is not required for cloud cover analysis: we require a transect to comprise at least 100 km of consecutive high-cloud-screened profiles, thus ensuring a long enough transect length to capture most of the contributions to cloud cover from clouds of different sizes. A transect may be less than 100 km, and therefore excluded from the cloud length dataset, because a) it "clips" the edge of a 5° x 5° gridbox, b) high cloud screening eliminates a portion of the transect so that the remaining segment lengths are shorter than 100 km, or c) a portion of transect is land. However, even transects longer than 100 km have a maximum length (~550 km) imposed by 5° x 5° gridding of the data. For every cloud length calculated we retain the length of the transect containing the observed cloud, and use this information to formulate a simple correction to the size distribution to account for this upper limit cut-off as follows,

$$n_{corr}(L)dL = n(L)dL[L_{tran}/(L_{tran} - L_{min})] \quad (1)$$

where $n_{\mathrm{corr}}(L)$ is the corrected cloud count, L_{tran} is the mean of the binned transect lengths, L_{min} is the bin minimum cloud length, $n(L)\,dL$ is the number of clouds sampled with sizes between L and $L + dL$. To help elucidate the contributions of optically-thin and optically-thick profiles to clouds of a given size, we construct size distributions for "majority

optically-thick" (contiguous cloudy profiles for which over 90% of contributing profiles are optically-thick) and "majority optically-thin" (over 90% of contributing profiles are optically-thin). The cloud length dataset is a subset of the dataset described in Section 2.3.1, and is comprised of approximately three times fewer profiles (cf. Fig. 4a and 4b) because of the minimum transect length restriction.

3.0 Results

3.1 Cloud Cover

High-cloud-screened marine low-cloud cover (f_{cld}) is at a minimum throughout the deep tropics, and is at a maximum in the northern hemisphere and southern hemisphere storm-track regions, with additional maxima in the stratocumulus regions on the eastern side of the oceanic subtropical highs (Fig. 5a). Values range from 0.10 to greater than 0.80, with a two-year, domain-mean of 0.50. The spatial pattern of cloud cover is similar to climatologies from surface observations (Warren et al., 2010, Climatic Atlas of Clouds Over Land and Ocean, available from *http://www.atmos.washington.edu/CloudMap*) and remote sensing [*Rossow and Schiffer*, 1999]. Optically-thin low-clouds are present in 10-30% of profiles over the non-polar oceans, with no strong geographic variation (f_{thin}; Fig. 5b). When expressed as the fraction of marine low-cloud profiles that are optically-thin ($f_{thin,cld}$), a clear spatial pattern emerges, with maxima in the trade wind cumulus regions, and minima in persistent stratocumulus and storm-track regions (Fig. 5c). The two-year mean value of $f_{thin,cld}$ is 0.45 demonstrating that almost half of all marine low-clouds appear to have optical depths less than or equal to 3. Interestingly, this picture from CALIPSO is consistent with the cumulative cloud optical depth distribution from MODIS (Fig. 2), although as we shall see the cloud scale that must be resolved in order to capture the optically-thin clouds makes an accurate assessment with MODIS questionable.

A strong negative correlation between $f_{thin,cld}$ and f_{cld} exists at both monthly and annual timescales (Fig. 6). In the trade wind regions, where marine low-cloud cover is lower than 0.25 [Fig. 5a, and *Medeiros et al.*, 2010], it is remarkable that consistently greater than 80% of the clouds are optically-thin. In regions typical of marine stratocumulus, where nighttime marine low-cloud cover exceeds 0.80, $f_{thin,cld}$ is consistently

lower, with values of 0.30 or less being typical. The presence of a large amount of marine low-cloud that is optically-thin on the scale of the relatively small CALIOP footprint is surprising and warrants further investigation. We devote much of this paper to analyzing these optically-thin clouds. However, we should note that this result is consistent with the TOA albedo from Clouds and the Earth's Radiant Energy System (CERES) data (available from *http://eos.atmos.washington.edu/cgi-bin/ceres/disp.pl?ceres.alb.ann.d)* of the trade wind regions being quite low (typically 0.16) despite cloud coverage in the trade wind regions of 0.20–0.25. Given observed trade wind TOA albedo and cloud cover, and using a simple cloud albedo – cloud optical depth relation [*Lacis and Hansen*, 1974] and a simple TOA albedo model (see Section 4), we estimate that cloud optical depth τ_{cld} would need to be 2.8–3.5 to produce the observed TOA albedo, if all clouds have the same τ_{cld}. While the prevalence of optically-thin clouds may appear surprising, it is consistent with regional albedo observations.

3.2 Cloud Length Distribution

Here, we examine the properties of marine low-clouds, and especially optically-thin clouds, as a function of their horizontal scale. Results presented in this section are derived from analysis of cloud entities, i.e., a series of consecutive high-cloud-screened, full-resolution CALIOP profiles containing a cloud at altitudes lower than 3 km, which are bounded on each end by a cloud-free profile. We find that cloud length distributions approximately follow a power law fit ($n(L) = \alpha L^{-\beta}$), where n(L) is the number of clouds of size L to L+dL, L is the bin center, and α and β are constants, consistent with previous studies [*Zhao and Di Girolamo*, 2007; *Wood and Field*, 2011; *Benner and Curry*, 1998]. For β = 2, each logarithmic size interval (e.g., 100m-1km, 1km-10km, etc.) contributes

360 equally to total cloud cover and $\beta > (<) 2$ implies that the distribution is weighted towards
361 smaller (larger) clouds [*Wood and Field*, 2011].
362 For the CALIOP dataset comprising both optically-thin and optically-thick low-
363 clouds, the size distribution is well fitted by a single power law with $\beta = 2.03 \pm 0.06$ (error at
364 2σ level). This is higher than the value of 1.66±0.04 reported by *Wood and Field*, [2011]
365 for a near-global cloud dataset comprising aircraft and satellite data. One explanation may
366 be differences in cloud sampling at the low and high ends of the size distribution. Although
367 *Wood and Field* [2011] aircraft data have a higher resolution than CALIOP, ~100 m
368 compared to 335 m, respectively, the aircraft did not sample regions where cumulus is the
369 dominant cloud type [*Wood and Field*, 2000, 2011]. Further, CALIOP may undersample
370 large clouds as the upper cloud length limit for this study is ~550 km compared to ~4000
371 km in *Wood and Field*, [2011]. Thus, our dataset tends to sample smaller clouds on
372 average, and smaller clouds tend to have larger exponents (see Fig. 12 in *Wood and Field*,
373 [2011]).
374 "Majority optically-thin" clouds (defined in Section 2.3.2) constitute most of the
375 clouds smaller than 4 km, whereas larger clouds have a greater contribution from optically-
376 thick profiles (Fig. 7). This highlights the increasing importance of optically-thin clouds as
377 clouds become smaller.
378 To further explore differences in cloud length distributions, we focus on three
379 specific cloud regimes (Table 3): 1) a region of persistent stratocumulus off the California
380 coast; 2) a tropical Pacific stratocumulus to cumulus (Sc-Cu) transition region; 3) a trade
381 wind cumulus region of the tropical Pacific. Cloud length distributions for the regions of
382 stratocumulus and Sc-Cu transition follow a β less than 2 power law fit with values of
383 1.81±0.08 and 1.68±0.09, respectively, indicating that large clouds dominate cloud cover

(Fig. 7, inset). As expected, the trade wind cloud length distribution has β greater than 2 (2.49±0.25) and is dominated by clouds with length less than 2 km, consistent with prior studies of trade wind cumulus [*Benner and Curry,* 1998; *Zhao and Di Girolamo,* 2007]. Since trade wind regions consist largely of optically-thin clouds (Fig. 5c), these results paint an emerging picture of small marine low-clouds being optically-thin. This has implications for the remote sensing of cloud and aerosol properties given current sensor resolution for most passive satellite instruments used to construct cloud climatologies.

3.2.1 Cloud Length at Median Cloud Cover

We define cloud length at median cloud cover (L_{50}) for each of the three cloud categories (marine low-cloud, "majority optically-thin" cloud, "majority optically-thick" cloud) such that clouds with lengths up to L_{50} contribute 50% to cloud cover for that category. Regions with the smallest coverage of low-cloud are associated with smaller L_{50} values (cf. Fig. 5a and Fig. 8a), with L_{50} less than 1 km in trade wind cumulus regions and L_{50} greater than 50 km in stratocumulus regions. Our results for the trades are qualitatively consistent with a recent study in the tropical western Atlantic trade wind region reporting L_{50} of 2 km using high-resolution passive visible satellite data [*Zhao and Di Girolamo,* 2007]. Additionally, we observe an inverse relationship between marine low-cloud L_{50} and β (not shown) also noted by *Wood and Field,* [2011], indicating that variations in β explain almost one-third of the observed geographical variance in L_{50}. Instances of horizontally extensive (greater than 10 km) "Majority optically-thin" clouds are observed (Fig. 7) but with an order of magnitude smaller frequency than "Majority optically-thick" clouds at these lengths. Most notably, poleward of 40 ° in both hemispheres, "Majority optically-thin" L_{50} is greater than 10 km (Fig. 8b), Cloud cover in these regions is mainly Sc (Warren et al., 2010, Climatic Atlas of Clouds Over Land and Ocean

409 http://www.atmos.washington.edu/CloudMap/WebO/index.html). These large L_{50} values
410 are consistent with the dimensions of open cells within Sc, [*Wood and Hartmann*, 2006],
411 characterized by regions of low optical depth or LWP. "Majority optically-thick" and
412 "majority optically-thin" L_{50} maps support our earlier statement that optically-thin marine
413 low-clouds are in general, smaller in size than optically-thick marine low-clouds (Fig. 8b
414 and 8c).
415
416 3.2.2 Cloud Length Distribution from HSRL
417 The horizontal separation between consecutive CALIOP pulses is 0.335 km but
418 many small cumuli are only a few tens to hundreds of meters in size [*Hozumi et al.*, 1982*;*
419 *Wielicki and Welch*, 1986; *Koren et al.*, 2008]. The inter-profile region not sampled by
420 CALIOP may be populated with one or more small clouds with clear gaps, or may be
421 entirely clear. For our cloud length estimates, if two consecutive profiles are flagged as
422 cloudy we assume that the intervening atmosphere is cloudy, and this could lead to CALIOP
423 overestimating cloud lengths. To examine the extent to which this may occur, we compare
424 spatially matched CALIOP and HSRL cloud length data, noting that HSRL footprints are
425 contiguous. Data are from the tropical western Atlantic trade wind region (Section 2.2 for
426 dataset description).
427 A minimum transect length criterion of 30 km is applied to the HSRL-CALIOP
428 comparison dataset for estimation of cloud lengths. This is shorter than for our analysis
429 from CALIPSO alone (100 km), because the ± 15 minute temporal matching limits transect
430 lengths to less than 200 km, and we find that a minimum length requirement of 100 km
431 would greatly reduce the data available for comparison in what is already a relatively small
432 dataset of collocated data. However, this work (Fig. 8) and other studies indicate that
433 characteristic cloud lengths in the tropical western Atlantic region are substantially smaller

than 30 km [*Benner and Curry*, 1998; *Wielicki and Welch*, 1986; *Zhao and Di Girolamo*, 2007], and so our reduced transect length threshold for the HSRL/CALIPSO size distribution estimates should not produce large problems.

The CALIOP and HSRL cloud length distributions are broadly similar for sizes larger than 1 km, but CALIOP samples more large clouds (Fig. 9). This is because HSRL is able to sample smaller clouds than CALIOP can resolve: these clouds comprise 55% of the clouds sampled by HSRL. Sub-sampling HSRL as CALIOP (i.e., we subsample HSRL profiles every 335 m) shifts the HSRL cloud length distribution to larger sizes, closely matching the CALIOP data (Fig. 9), suggesting that the size distribution differences at cloud lengths smaller than 1 km are primarily due to sparse sampling by CALIOP rather than FOV size differences (HSRL FOV is 60 m; CALIOP FOV is 90 m). CALIOP and HSRL region mean f_{cld} values (0.24 and 0.31, respectively) agree to within 2 standard deviations, but $f_{\mathrm{thin,cld}}$ values do not agree, being 0.89 (CALIOP) and 0.61 (HSRL). This effect cannot be due to the relative along-track sparsity of CALIPSO sampling. Differences in HSRL and CALIOP cloud detection algorithms may be partly responsible for the $f_{\mathrm{thin,cld}}$ disparity (e.g., the HSRL layer detection method may not be well suited to detecting attenuated surface returns). Another likely cause is the narrow HSRL FOV (8 m across-track compared with 60 m along-track), giving rise to the possibility that HSRL will miss some small clouds that lie on either side of the HSRL FOV, but which lie inside the CALIOP FOV (see schematic in Fig. 9, inset). Since smaller clouds tend to be optically-thin, the clouds missed by HSRL are likely to be optically-thin.

The HSRL size distribution in Fig. 9 shows a roll-off at cloud lengths below about 0.5 km. This may be a hint that there exists some lower limitation to the cloud length of the smallest clouds, i.e., a scale break in the cloud length distribution, and this length is

458 consistent with the typical length scale of turbulent eddies in the boundary layer. Without
459 further evidence from observations and models we cannot be sure if the scale break is a real
460 physical feature or reflects sampling a mixture of distributions on different days, but very
461 high-resolution large eddy simulations could be used to examine this. We note that one
462 high-resolution Landsat satellite study [*Sengupta et al.*, 1990] reported a scale break in
463 cumulus cloud length distribution at 1 km, with larger (smaller) β observed for larger
464 (smaller) clouds. The scale break was observed at a larger size (1 km) than in the HSRL
465 data shown here (~500 m). Such a scale break is not a universal feature in trade cumulus
466 [*Zhao and Di Girolamo*, 2007]. Further studies with high-resolution airborne lidar would
467 be helpful to understand any physical limits to the population of the smallest clouds.
468 Cloud length at median f_{cld} for the matched HSRL/CALIOP data indicate that L_{50} is
469 1.3 km for HSRL, and L_{50} is 1.7 km for CALIOP. The L_{50} value from two years of CALIOP
470 data for this region is 1.3 km, close to the matched dataset value. We therefore believe that
471 the conclusions we derive from the HSRL/CALIOP comparison are somewhat
472 representative of trade cumulus regions throughout the tropics.
473
474 3.2.3 Cloud Length Distribution and Optically-thin Cloud Cover Variation
475 Another approach to examine how optically-thin profiles are distributed among
476 clouds of different sizes is to bin, as a function of cloud length L, the fraction of cloudy
477 profiles that are optically-thin ($f^{L}_{thin,cld}$). For this we use the entire CALIOP cloud dataset
478 (1.7 million cloud entities). Surprisingly, the function $f^{L}_{thin,cld}$ is almost region-invariant
479 (Fig. 10). As cloud length increases, the fraction of optically-thin profiles comprising that
480 cloud decreases. Clouds of a given horizontal size possess a similar fraction of optically-
481 thin elements regardless of whether they occur in regions dominated by trade wind cumulus

482 or stratocumulus. Approximately 50% of profiles comprising clouds of size L~15 km, as
483 determined by CALIOP, are optically-thin. Clouds smaller than 2 km are almost entirely
484 optically-thin, whereas clouds larger than 100 km are less than 20% optically-thin. A
485 similar relationship is observed in the HSRL data (not shown), although HSRL $f^L_{thin,cld}$
486 curve is shifted to smaller cloud lengths, for reasons discussed in the preceding section.
487 The near universal nature of $f^L_{thin,cld}$ would be explicable if each region essentially
488 experiences low-clouds of all type, from small cumulus to relatively large sheets of
489 stratocumulus. Visual inspection of visible imagery suggests that this is a reasonable
490 supposition. Surprisingly, these cloud types appear to have very similar characteristics in
491 terms of their optical thickness distribution, regardless of location. Clearly, however, the
492 frequency with which each region experiences clouds of different sizes varies dramatically
493 from region to region. This result leads us to ask whether geographical variations in the
494 fraction of clouds that are optically-thin might be largely explained by regional differences
495 in the distribution of clouds of all sizes.
496 To test this, we make an estimate of the optically-thin fraction of marine low-clouds
497 ($\tilde{f}_{thin,cld}$) using a single $f^L_{thin,cld}$ function based on the entire non-polar ocean dataset
498 (Fig. 10) together with the 5×5° binned two-year cloud length distributions $n(L)$ as,

499 $$\tilde{f}_{thin,cld} = \frac{1}{\int_{L_{min}}^{L_{max}} L\, n(L)\, dL} \int_{L_{min}}^{L_{max}} f^L_{thin,cld} L\, n(L) dL \qquad (2)$$

500 where $L_{\max/\min}$ is the upper/lower CALIOP size range limit and L is the bin center cloud
501 length. We find that over non-polar oceans, and separately, over the tropics, the cloud
502 length distribution alone explains three-quarters of the variance in $f_{\text{thin,cld}}$ (R^2 = 0.73 and
503 0.77, respectively). What this result tells us is that knowledge of how the marine low-cloud
504 length distribution of all clouds varies is sufficient to accurately predict the geographical

505 variation in the optically-thin fraction of clouds across most of the ocean. This is important
506 because it allows us to connect optically-thin clouds with the population of all clouds, and
507 suggests that the processes controlling optically-thin clouds should not be considered as
508 independent of the processes controlling low-clouds in general.
509
510 3.3 Cloud Vertical Structure
511 Knowing the vertical distribution of cloud condensate is important for radiative transfer
512 calculations and for model parameterization of cloud overlap. Vertically-resolved (60 m)
513 optically-thin and optically-thick CTH, optically-thin cloud base height (CBH), and
514 optically-thin cloud-layer depth are presented for each of the three cloud regimes previously
515 mentioned (Section 3.2; Table 3). Note that only CTH can be observed for optically-thick
516 clouds as, by definition, the signal is fully attenuated by the cloud. The dynamical
517 processes associated with each cloud regime are as follows: The vertical development of
518 marine stratocumulus is suppressed by subsidence associated with either the descending
519 branch of the Hadley circulation, or subsiding air masses associated with mid-latitude
520 cyclones, depending upon location. As a result, the marine stratocumulus layer is capped by
521 a strong temperature inversion, resulting in extensive low-clouds [*Klein and Hartmann*,
522 1993]. As the stratocumulus air mass moves equatorward it is advected over warmer sea-
523 surface temperatures (SSTs), surface latent heat fluxes increase, and the subsequent
524 transition to a cumulus regime is described by the deepening-warming mechanism proposed
525 by *Wyant and Bretherton* [1997]. Consistent with a deepening marine boundary layer from
526 stratocumulus to trade cumulus, both optically-thin and optically-thick CTH distributions
527 peak at higher altitudes transitioning from a stratiform to a convective type cloud regime
528 (Fig. 11a-11c).

529 In the stratocumulus region, optically-thick CTH peaks at twice the altitude
530 observed for optically-thin clouds (1.2 km and 0.6 km, respectively). Although cloud cover
531 in stratocumulus regions is dominated by optically-thick cloudy profiles (Fig. 5c), optically-
532 thin cloudy profiles comprise greater than 95% of clouds up to 4 km in size (Fig. 10),
533 suggesting that small clouds typically have lower CTH than larger, optically-thicker clouds.
534 Noting that estimates of stratocumulus depth range from 200-300 m in the subtropics and
535 tropics [*Wood*, 2011], and that optically-thin cloud-layers preferentially reside in the lowest
536 1 km with mean depth of 200 m (Fig. 12a), we suggest that incidences of optically-thin
537 CTH less than 1 km in this stratocumulus region, are separate cloud entities from the
538 optically-thicker clouds with CTH greater than 1 km. Many of these likely reflect
539 expansive collapsed boundary layers and fog layers (note occurrence of very low-cloud
540 bases in Fig. 11d and data along the 1:1 line in Fig. 12a) that occur periodically in regions
541 dominated by marine stratocumulus [*Ackerman et al.*, 1993; *Christensen and Stephens*,
542 2011].

543 As would be expected given the weakening of the capping inversion and deepening
544 of the marine layer in the transition from stratocumulus to cumulus, optically-thin and
545 optically-thick CTH distributions are shifted upwards, relative to the stratocumulus regime
546 (cf. Figs. 11a and 11b). Cloud cover remains largely optically-thick, but there is an
547 increasing fraction of optically-thin layers. In contrast to the stratocumulus region, the tops
548 of these layers tend to occur at altitudes closer to the optically-thick layers, suggesting that
549 the optically-thin clouds in the transition region may be largely associated with thinning
550 stratocumulus and stratus layers, and remnants of dissipating stratocumuli near the top of
551 the boundary layer.

552 In the trade wind cumulus region (Fig. 11c and 11f), the modal heights for optically-
553 thin and optically-thick cloudy profiles are again at different levels (0.8 and 2 km
554 respectively). Optically-thin profiles dominate the cloud cover in this regime ($f_{\text{thin,cld}}$ is
555 0.84), and clouds are not horizontally extensive (L_{50} is 0.96 km). Despite having modes at
556 distinct levels, optically-thin and optically-thick CTH are observed at all levels up to 3 km
557 (Fig. 11c). Peak optically-thin CBH is ~300 m (Fig. 11f). Detrained elements from
558 optically-thick clouds may account for a large proportion of optically-thin clouds at
559 altitudes greater than 1 km, but the mode in optically-thin clouds below 1 km probably
560 consists of small cumuli and associated fragments of clouds with insufficient buoyancy to
561 grow in stature. An aerial photograph of a trade wind cloud field (Fig. 13) highlights the
562 wide range of horizontal and vertical cloud dimensions found in trade wind regions.
563 Notable is the prevalence of tenuous, wispy clouds with limited vertical extent, along with
564 optically thicker clouds, although the latter are less numerous. The bimodal nature of the
565 combined optically-thin and optically-thick cumulus CTH distributions (sum of both
566 distributions, not shown) agrees well with high-resolution (90 m) satellite observations of
567 trade wind cumulus CTH [*Genkova et al.*, 2007], and with a large-eddy simulation (LES)
568 CTH distribution for a non-precipitating trade cumulus case [*Siebesma et al.*, 2003]. This
569 encouragingly suggests that LES is a useful tool to examine macrophysical properties of
570 optically-thin clouds that are the dominant cloud type in the trade wind cloud regimes.
571 The optically-thin cloud-layer thickness distributions (Fig. 12 insets) are similar for
572 all three regions. The drop-off in frequency of occurrence of layers less than 180 m may be
573 an artifact of the increase in the nighttime optical depth detection threshold for shallow
574 layers, i.e. the threshold is 0.03 for layers greater than 180 m, and 0.1 for shallower layers
575 (Section 2.1). We note, however, that optically-thin cloud-layer depth may be

576 overestimated by CALIOP VFM: if a cloud partially fills a 60 m height bin yet has an
577 optical depth greater than 0.1, the entire 60 m bin will be classified as cloudy. This high
578 bias will affect thin layers more than thick layers, in a relative sense. For example, a 60 m
579 optically-thin cloud partially filling two vertically adjacent 60 m bins, will register as 120 m
580 in depth, an error of 100%, whereas, an optically-thin cloud-layer occupying four 60 m bins,
581 and partially-filling a fifth bin by 50% will have a layer depth relative error of ~11%.
582 Conservatively assuming the maximum error of 60 m in layer depth yields a 30% potential
583 overestimate of mean optically-thin cloud-layer depth. Irregular or inhomogeneous clouds
584 e.g., trade cumulus, will be most prone to this error. A recent LES study investigating the
585 effects of cumulus cloud irregularity on cloud overlap quantified the effect of partially filled
586 model levels as a function of model vertical resolution [*Neggers et al.*, 2011]. Employing
587 their formulation at CALIOP VFM cloud-layer boundary detection resolution (60 m)
588 produces a high-bias estimate of 28%, which is very similar to our own estimate.
589

4.0 Discussion

Our findings point to a prevalence of optically-thin low-clouds over the oceans, even at the scale of individual CALIOP lidar profiles. While this might be expected at the scale of typical moderate resolution passive visible remote sensors used to construct cloud climatologies, our prior expectation was that most of the optically-thin cloudy pixels from these moderate-resolution passive sensors would be partially filled by small cumulus covering only a small fraction of the pixel, and that the clouds themselves might have considerably higher optical thicknesses than the pixel as a whole. This appears not to be the case, and it prompts us to ask whether even the CALIOP FOVs are partially filled with yet smaller clouds. Given that there are many single-profile cloud entities in the CALIOP dataset (Figs. 7 and 9), it is possible a significant fraction of these profiles are partially filled.

The cloud within any CALIOP partially filled field of view (pFOV) could be optically-thick or optically-thin. Based upon CALIOP data alone, we cannot diagnose whether or not a cloudy FOV is partially cloud-filled, nor can we determine if the cloud-filled part is optically-thick or optically-thin. Classifying a pFOV as optically-thin when the cloud intercepted is optically-thick cloud will lead to an overestimate of $f_{\mathrm{thin,cld}}$. To investigate the frequency of pFOVs, and whether or not the clouds partially filling the lidar FOVs are optically-thick, we employ a simple bounded cascade fractal model.

4.1 Bounded Cascade Model Description

An in-depth description of the model is presented by *Marshak et al.* [1994] and its application to simulating one-dimensional cloud fields is provided by *Wood and Field* [2011]. A brief description follows. A one-dimensional multiplicative cascade broken cloud field is generated by initially assuming a uniform value of a cloud property; here,

615 optical depth. The field is bisected, and each half is scaled by a factor $1 \pm w_i$, with the
616 gaining half chosen at random. This is repeated for each half, and so on, with weighting
617 factors (w_i) calculated for each step i as,

618 $$w_i = \frac{(1-2p)}{2^{H(i-1)}} \quad (3)$$

619 where p ($0 < p < 0.5$) controls the intermittency of the resulting optical depth field, and H (0
620 $< H < \infty$) is a scaling factor representing the smoothness of the field. This simple model has
621 displayed skill in representing scaling properties of marine stratocumulus liquid water
622 content [*Marshak et al.*, 1997; *Davies et al.*, 1999], and cloud length, on a global scale
623 [*Wood and Field*, 2011]. Specifically, it is shown in the latter case, the power law exponent
624 β in the cloud length distribution is inversely related to the value of H, such that smooth
625 fields (large H) are associated with more large clouds and low β, and vice versa.

626 We focus our investigation on our representative tropical Pacific trade wind region
627 (Table 3) because the trades have the smallest marine low-clouds (Fig. 8a) and are therefore
628 likely to be the most prone to the partially filled FOV problem. Experimentation showed
629 that model settings that best simulate CALIOP observations are $p = 0.05$, $H = 0.015$, with
630 scene mean optical depth (which is also a specified input variable) set to 3.5, and were
631 selected as follows. Since H is closely related to β (Fig. 15; *Wood and Field*, [2011]), we
632 vary H to match CALIOP observed β. Optical depth thresholds for CALIOP cloud
633 detection ($\tau_{cld,thresh}$), and optically-thin cloud ($\tau_{thin,thresh}$) are 0.03 and 3 respectively. We also
634 vary p to match observed CALIOP trade wind region mean f_{cld} and $f_{thin,cld}$ as closely as
635 possible. Finally, scene mean optical depth is adjusted such that TOA albedo estimated
636 from model τ_{cld} values, falls within the range of CERES values for this region. Calculation
637 details are presented in full in Table 4. Output is from 100 model runs, each with 17
638 cascade steps and 2^{18} individual data points representing a ~700 km transect (each model

639 data point represents ~2.8 m horizontally). Each CALIOP lidar FOV (90 m) is comprised
640 of 32 model data points, and consecutive FOVs are separated by 335 m. We correct all
641 modeled cloud length distributions for sampling bias associated with clouds approaching the
642 limited transect length as per (1).
643
644 4.1.2 Model Simulation of Observed Cloud Properties
645 The model demonstrates reasonable skill in generating realistic representations of
646 CALIOP observed cloud properties (Table 4), suggesting that optically-thin cloud behavior
647 is broadly consistent with a power law scaling of optical depth. For comparison, we also
648 sample the model output simulating MODIS and HSRL FOV (1 km and 60 m (along-track
649 dimension), respectively). All HSRL model output is analyzed using CALIOP $\tau_{cld,thresh}$ and
650 $\tau_{thin,thresh}$ thresholds. We set MODIS $\tau_{cld,thresh}$ to be 0.4 (Ackerman et al., 2008), with
651 $\tau_{thin,thresh}$ as for CALIOP. Unexpectedly, model simulated MODIS f_{cld} is a factor of two
652 *lower* than CALIOP and HSRL simulated f_{cld} (Table 4). Setting MODIS $\tau_{cld,thresh}$ to 0.2 and
653 0.6 produces model simulated MODIS f_{cld} values of 0.24 and 0.12, respectively. We
654 therefore suggest that overestimation of cloud cover by passive sensors (e.g., *Zhao and Di*
655 *Girolamo*, [2006]) may not necessarily always occur. Rather, the bias depends sensitively
656 upon cloud length and the reflectance threshold applied.
657 As instrument resolution increases (footprint size decreases), each simulated size
658 distribution is shifted to smaller sizes (Fig. 14). We note that the model-simulated HSRL
659 cloud length distribution, since it is derived from a bounded cascade, does not reproduce the
660 observed gradual roll-off to a flatter size distribution at cloud lengths smaller than ~500 m
661 seen in the tropical western Atlantic trade wind region (Fig. 9). Interestingly, all simulated
662 cloud length distributions produce similar β values to CALIOP, a result also noted by *Wood*
663 *and Field* [2011], whereby the cloud length distribution is not strongly sensitive to sensor

664 resolution when the domain to pixel ratio approaches 1000. For this model analysis
665 "domain" is ~ 700 km, and "pixel" refers to FOV size. The domain to pixel size ratio is
666 therefore much greater than 1000 for model clouds sampled like CALIOP and HSRL, and is
667 close to 1000 in the case of MODIS, and so we would not expect β to be very different
668 across the sensors.

669 The HSRL has a pulse repetition frequency of 200 Hz, and so prior to averaging, the
670 data have less than 1 m along-track sampling resolution for an aircraft flight speed of 120 m
671 s^{-1}. Although onboard averaging means that we do not actually have observations at this
672 resolution from HSRL, it would be interesting to see whether size distributions using higher
673 resolution cloud masks would be shifted to even smaller sizes. The model results suggest
674 that observations at CALIOP and HSRL resolution both miss finer scale cloud length
675 variations, and overestimate cloud lengths (Fig. 14). Additionally, even cloud cover
676 estimates made at CALIOP and HSRL resolution may overestimate f_{cld} by a factor of two in
677 trade wind regions (Table 4). Although these model results require verification, especially
678 model behavior at small scales, we note that a four-fold overestimate in f_{cld} was calculated
679 from high-resolution (15 m) trade Cu observations when sensor resolution was degraded to
680 1 km [*Dey et. al.,* 2008]. Indeed, this suggests that the very concept of cloud cover may be
681 so sensitive to sensor resolution and detection sensitivity in the trades that it serves no
682 useful function in these regions. For lower resolution sensors (e.g., MODIS) such small-
683 scale clouds produce cloud-contamination in clear FOVs [*Koren et al.,* 2007], biasing clear-
684 sky retrievals.

685
686 4.2 Partially Filled Fields of View

687 As previously mentioned, a CALIOP FOV may be misidentified as optically-thin if
688 partially filled by an optically-thick cloud. We use the model to identify CALIOP FOVs

689 that are partially cloud-filled, i.e., not all 32 optical depth values comprising the simulated
690 FOV exceed the threshold for cloud detection ($\tau_{cld,thresh}$). We also note whether or not the
691 mean optical depth of both an entire pFOV and the cloud-only segment of the pFOV are
692 less than $\tau_{thin,thresh}$. Inconsistencies between the two values will highlight pFOVs mislabeled
693 as optically-thin when the cloudy sub-pixel is actually optically-thick cloud. Results are
694 binned by cloud length.

695 The fraction of FOVs that are partially cloud-filled decreases from 100% to 84%
696 across the cloud length range (Fig. 15, circles). CALIOP detected cloud entities consisting
697 of a single profile are therefore almost all likely to be partially filled FOVs. In addition, the
698 bin median pFOV cloud fraction, i.e., fraction of a pFOV that is cloud, increases with cloud
699 length, ranging from 0.30 to 0.75 (Fig. 15, squares). The smallest cloud length bin (bin
700 center size is 0.5 km) is wholly populated with partially cloud-filled FOVs, however, the
701 mean optical depth of the cloud-only segment within each FOV is less than $\tau_{thin,thresh}$, and the
702 cloud is therefore correctly classified as optically-thin. Across all cloud lengths, the cloud-
703 only segment of pFOV exceeds 97% optically-thin (Fig. 15, diamonds) resulting in few
704 instances of pFOV mislabeled as optically-thin. Summing in quadrature the fraction of
705 pFOV that are misclassified for each size bin, we conclude that potential overestimate of
706 $f_{thin,cld}$ is at most 7% for this cloud regime. In addition, combining the cloud length
707 distribution with the fraction of FOVs that are partially cloud-filled (Fig. 15, circles) and bin
708 median pFOV cloud fraction (Fig. 15, squares) we estimate that the overestimate in f_{cld} that
709 is directly attributable to partially cloud filled FOVs, is approximately one-third. Based
710 upon this model output which is designed to simulate typical trade wind cumulus
711 conditions, we would conclude that the majority of cloudy CALIOP profiles are indeed
712 partially cloud-filled. Rapid fluctuations of cloud particle concentration on scales ~10 m

713 have been measured in situ [*Pawlowska et al.,* 1997], suggesting that this conclusion is
714 physically realistic.

715

716 4.3 Additional Applications of Cascade Model Output

717 4.3.1 Are Optically-thin Clouds Adiabatic?

718 We analyze the model output to investigate the extent to which optically-thin clouds
719 might be considered adiabatic, i.e., have liquid water path (*LWP*) values determined by
720 temperature, pressure and cloud thickness alone. Liquid water path for an adiabatic cloud is
721 proportional to cloud-layer depth (h) squared, the adiabatic rate of increase of liquid water
722 with respect to height (assumed to be 2×10^{-3} g m^{-3} km^{-1}) [*Albrecht et al.*, 1990], and the
723 adiabatic fraction (f_{ad}), is defined as the ratio of observed *LWP* to adiabatic *LWP*, which
724 here we assume to be 1. Using model simulated optically-thin cloud optical depth for a
725 trade wind region as before, and assuming a cloud droplet effective radius (r_e) of 10 μm, we
726 estimate $LWP = 2/3\tau\rho_L r_e$ [*Stephens*, 1994], where ρ_L is liquid water density, and derive
727 corresponding adiabatic cloud-layer depth, h. The simulated adiabatic layer depth
728 distribution (not shown) indicates that depths are on the order of a few 10s of meters, with
729 90% of the values being less than 90 m, much thinner than observed. In addition, if this
730 *LWP* is evenly distributed over a 60 m layer, we estimate that $f_{ad} \sim 0.09$; alternatively, if τ_{cld}
731 is 0.1, layer depth corresponding to an adiabatic *LWP* is 25 m. Therefore, we conclude that
732 the optically-thin cloud-layers are not adiabatic, but are more likely to be diluted cloud
733 fragments. This is consistent with effects of entrainment on marine layer clouds (e.g.,
734 *McFarlane and Grabowski* [2007]). Stochastically-controlled entrainment events
735 essentially dictate the properties of shallow trade cumulus clouds [*Romps and Kuang*,
736 2010].

737

738 4.3.2 Optically-thin Cloud Contribution to TOA Cloud Albedo

739 We have shown that optically-thin clouds comprise almost one-half of all marine
740 low-clouds over non polar oceans. To investigate the magnitude of their contribution to
741 TOA albedo (α^{TOA}) in trade wind regions, we estimate clear-sky α^{TOA} (Table 4), and
742 compare that value to CERES α^{TOA}, to quantify cloud albedo for various trade wind regions.
743 The optically-thin low-cloud contribution to cloud albedo can be estimated from model
744 simulated optically-thin cloud optical depth converted to optically-thin low-cloud albedo, as
745 outlined in Table 4. We conclude that for trade wind regions with observed $f_{thin,cld}$ greater
746 than 0.80, and f_{cld} ~0.20 – 0.30, optically-thin low-clouds may contribute 10-25% to the
747 total cloud albedo.

748

749 **5.0 Summary of Findings**

750 Analysis of two years of CALIOP nighttime data indicates that 45% of marine low-
751 clouds with tops lower than 3 km, over the non-polar oceans, appear to be optically-thin, in
752 that they do not fully attenuate the CALIOP lidar signal. Few observational data, other than
753 this work, are available on the physical nature of these clouds. Key results from our
754 analysis are as follows:

755 1) Over the non-polar oceans, optically-thin clouds comprise 0.25 – 0.75 of marine
756 low-clouds with cloud top height below 3 km, with a mean of 0.45;

757 2) The optically-thin fraction of marine low-cloud varies inversely with marine low-
758 cloud cover, and reaches a maximum (> 0.80) in trade wind regions;

759 3) Although the optically-thin fraction of low-clouds peaks in trade wind regions, the
760 absolute frequency of occurrence is almost constant over the non-polar oceans;

761 4) In trade wind regions, according to CALIOP, clouds smaller than 1.5 km contribute
762 over 50% of the cloud cover;

5) Optically-thin marine low-clouds are predominantly small clouds. The cloud length distribution of all clouds explains three-quarters of the geographical variance in the optically-thin fraction of marine low-clouds;

6) Over the non-polar oceans, optically-thin low-clouds have a mean cloud top height of 1.2 km and a mean thickness of 0.25 km. However, optically-thin cloud-layer depth may be overestimated by 30% due to cloud partially filling the 60 m vertical resolution CALIOP bins;

7) Collocated HSRL and CALIOP data for the tropical western Atlantic trade wind region reveal that some clouds are smaller than can be resolved at CALIOP resolution. This suggests that clouds, and especially optically-thin low-clouds, may exist globally on finer scales than reported herein;

8) A simple bounded cascade fractal model is used to represent a one-dimensional optical depth distribution for conditions representative of the trade wind regions. Analysis of model output, in conjunction with observations, suggests that:

   a) Optically-thin low-cloud properties are consistent with a power law scaling of optical depth;

   b) CALIOP fields of view partially filled with optically-thick low-cloud produce a potential 7% over-estimate in optically-thin fraction of marine low-cloud values in trade cumulus regions;

   c) Optically-thin cloud-layer thicknesses are not adiabatic with greater than 90% of simulated optically-thin cloud depths less than 90 m, while observations indicate much greater thicknesses;

   d) In trade cumulus regions, we estimate that optically-thin low-clouds contribute 10-25% of the albedo contributed by low-clouds, but a more

sophisticated quantification using radiative transfer modeling is required to confirm this.

Pincus et al. [2012] find that ISSCP and MODIS views of clouds are consistent for all but the thinnest clouds. However, because we find such a large fraction of clouds are optically-thin even at the much smaller footprint size of CALIOP, it leads us to ask whether the passive sensors are actually determining the coverage of the optically-thick or optically-thin clouds correctly. It is difficult to therefore conclude that we yet have a precise understanding of the shape of the true cloud optical depth probability distribution function on a global scale, and especially in trade wind regions.

Although CALIOP data do not provide any off-track spatial context for the cloud fields sampled, high sampling resolution in the along-track direction combined with vertically-resolved data, afford insights on the nature of optically-thin clouds. Suggestions for design of future combined active and passive remote sensors would include an array of lasers providing a swath of vertically-resolved data with, ideally, horizontal resolution of a few tens of meters or less, in the across-track and along-track directions, and collocated visible imagery with the same horizontal resolution. Such a configuration would provide collocated profiles of cloud properties, and high-resolution TOA reflectance data to better observe these optically-thin clouds, which comprise almost half of all marine low-clouds.

Acknowledgements

This work was supported by NASA award numbers NNX10AE59G and NNX10AN78G. We wish to thank Sarah Doherty for insightful comments which contributed greatly to the quality of this work.

812 **References**

813 Ackerman, A.S., O.B. Toon, and P.V. Hobbs (1993) Dissipation of marine stratiform clouds
814 and collapse of the marine boundary layer due to the depletion of cloud condensation
815 nuclei by clouds, *Science, 262*, 226-229, doi:10.1126/science.262.5131.226.
816 Ackerman, S., R. E. Holz, R. Frey, E. W. Eloranta, B. C. Maddux, and M. McGill (2008),
817 Cloud Detection with MODIS. Part II: Validation, *J. Atmos. Oceanic Technol., 25*,
818 1073-1086.
819 Albrecht, B. A., C. W. Fairall, D. W. Thomson, A. B. White, J. B. Snider, and W. H.
820 Schubert (1990), Surface-based remote sensing of the observed and the Adiabatic liquid
821 water content of stratocumulus clouds, *Geophys. Res. Lett., 17*, 89–92,
822 doi:10.1029/GL017i001p00089.
823 Albrecht, B. A., M. P. Jensen, and W. J. Syrett (1995), Marine boundary layer structure and
824 fractional cloudiness, *J. Geophys. Res., 100*, D7, 14,209-14,222.
825 Bender, F. A-M., R. J. Charlson, A. M-L. Ekman, and L. V. Leahy (2011), Quantification of
826 monthly mean, regional scale albedo of marine stratiform clouds in satellite
827 observations and GCMs, *J. Appl. Meteor. Clim.*, doi: 10.1175/JAMC-D-11-049.1
828 Benner, T. C., and J. A. Curry (1998), Characteristics of small tropical cumulus clouds and
829 their impact on the environment, *J. Geophys. Res., 103*, D22, 25,752-28,767.
830 Bucholtz, A. (1995), Rayleigh-scattering calculations for the terrestrial atmosphere, *Appl.*
831 *Opt., 34*, 2,765-2,773.
832 Charlson, R. J., A. S. Ackerman, F. A-M. Bender, T. L. Anderson, and Z. Liu (2007), On
833 the climate forcing consequences of the albedo continuum between cloudy and clear air,
834 *Tellus, 59*, 715-727, doi:10.1111/j.1600-0889.200700297.x.
835 Davies, A. B., A. Marshak, H. Gerber, and W. J. Wiscombe (1999), Horizontal structure of
836 marine boundary layer clouds from centimeter to kilometer scales, *J. Geophys. Res.*,
837 *104*, D6, 6,123-6,144.
838 Dey, S., L. Di Girolamo, and G. Zhao (2008), Scale effect on statistics of the macrophysical
839 properties of trade wind cumuli over the tropical western Atlantic during RICO, *J.*
840 *Geophys. Res., 113*, D24214, doi: 10.1029/2008JD010295.
841 Efron, B., and G. Gong (1983), A Leisurely Look at the Bootstrap, the Jackknife, and
842 Cross-Validation, *The American Statistician, 37*, 36-48.
843 Genkova, I., G. Seiz, P. Zuidema, G. Zhao, and L. Di Girolamo (2007), Cloud top height
844 comparisons from ASTER, MISR, and MODIS for trade wind cumuli, *Remote Sens.*
845 *Environ., 107*, 211-222.
846 Hair, J. W., C. A. Hostetler, A. L. Cook, D. B. Harper, R. A. Ferrare, T. L. Mack, W.
847 Welch, L. R. Izquierdo, and F. E. Hovis (2008), Airborne High Spectral Resolution
848 Lidar for profiling aerosol optical properties, *Appl. Opt., 47*, 6,734-6,752.
849 Harrison, E. F., P. Minnis, B. R. Barkstrom, V. Ramanathan, R. D. Cess, and G. G. Gibson
850 (1990), Seasonal variation of cloud radiative forcing derived from the Earth radiation
851 budget experiment, *J. Geophys. Res., 95*, 18687–18703.
852 Hartmann, D. L., M. E. Ockert-Bell, and M. L. Michelsen (1992), The Effect of Cloud Type
853 on Earth's Energy Balance: Global Analysis, *J. Climate, 5*, 1281–1304, doi:
854 10.1175/1520-0442(1992)005.
855 Hozumi, K., T. Harimaya, and C. Magono (1982), The Size Distribution of Cumulus Clouds
856 as a Function of Cloud Amount, *J. Meteor. Soc. Japan, 60*, 691-699.
857 Hunt, W.H., D. M. Winker, M. A. Vaughan, K. A. Powell, P. L. Lucker, C. Weimer (2009),
858 CALIPSO Lidar Description and Performance Assessment, *J. Atmos. Oceanic Technol.,*
859 *26*, 1214–1228, doi: 10.1175/2009JTECHA1223.1.

860 Kacenelenbogen. M., M. A. Vaughan, J. Redemann, R. M. Hoff, R. R. Rogers, R. A.
861 Ferrare, P. B. Russell, C. A. Hostetler, J. W. Hair, and B. N. Holben (2011), An
862 accuracy assessment of the CALIOP/CALIPSO version 2/version 3 daytime aerosol
863 extinction product based on a detailed multi-sensor, multi-platform case study, *Atmos.*
864 *Chem. Phy.*, *11*, 3,981-4,000, doi:10.5194/acp-11-3981-2011.
865 Kay, J. E., Hillman, B., Klein, S., Zhang, Y., Medeiros, B., Gettelman, G., Pincus, R.,
866 Eaton, B., Boyle, J., Marchand, R. and T. Ackerman (2012), Exposing global cloud
867 biases in the Community Atmosphere Model (CAM) using satellite observations and
868 their corresponding instrument simulators, *J. Climate*, doi:10.1175/JCLI-D-11-00469.1,
869 in press.
870 Klein, S. A., and D. L. Hartmann (1993), The Seasonal Cycle of Low Stratiform Clouds, *J.*
871 *Climate.*, *6*, 1,587-1,606.
872 Koren, I., L. A. Remer, Y. J. Kaufman, and Y. Rudich (2007), On the twilight zone between
873 clouds and aerosols, *Geophys. Res. Lett.*, *34*, L08805, doi:10.1029/2007GL029253.
874 Koren, I., L. Oreopoulos, G. Feingold, L. A. Remer, and O. Attaratz (2008), How small is a
875 small cloud?, *Atmos. Chem. Phys.*, *8*, 3,855-3,864.
876 Koren, I., G. Feingold, H. Jiang, and Orit Altaratz (2009), Aerosol effects on the inter-cloud
877 region of a small cumulus cloud field, *Geophys. Res. Lett.*, *36*, L14805,
878 doi:10.1029/2009GL037424.
879 Lacis, A. A., and J. E. Hansen (1974), A Parameterization for the Absorption of Solar
880 Radiation in the Earth's Atmosphere, *J. Atmos. Sci.*, *31*, 118-133.
881 Marshak, A., A. Davis, R. Cahalan, and W. Wiscombe (1994), Bounded cascade models as
882 nonstationary multifractals, *Phys. Rev. E, 49(1)*, 55-69.
883 Marshak, A., A. Davis, W. Wiscombe, and R. Cahalan (1997), Scale invariance in liquid
884 water distributions in marine stratocumulus. Part II: multifractal properties and
885 intermittency issues, *J. Atmos. Sci.*, *54*, 1,423-1,444.
886 Masonis, S. J., T. L. Anderson, and D. S. Covert (2003), A Study of the Extinction-to-
887 Backscatter Ratio of Marine Aerosol during the Shoreline Environment Aerosol Study,
888 *J. Atmos. Oceanic Technol.*, *20*, 1,388-1,402.
889 McFarlane, S. A., and W. W. Grabowski (2007), Optical properties of shallow tropical
890 cumuli derived from ARM ground-based remote sensing, *Geophys. Res. Lett.*, *34*,
891 L06808, doi:10.1029/2006GL028767.
892 Medeiros, B., L. Nuijens, C. Antoniazzo, and B. Stevens (2010), Low-latitude boundary
893 layer clouds as seen by CALIPSO, *J. Geophys. Res.*, *115*, D23207,
894 doi:10.1029/2010JD014437.
895 Neggers, R. A. J., T. Heus, and A. P. Siebesma (2011), Overlap statistics of cumuliform
896 boundary-layer cloud fields in large-eddy simulations, *J. Geophys. Res.*, *116*, D21202,
897 doi:10.1029/2011JD015650.
898 Pawlowska, H., J. L. Brenguier, and G. Salut (1997), Optimal Nonlinear Estimation for
899 Cloud Particle measurements, *J. Atmos. Oceanic Technol.*, *14*, 88-104.
900 Pincus, R. S., S. Platnick, S. Ackerman, R. Hemler, and R. Hofmann (2012), Reconciling
901 simulated and observed views of clouds: MODIS, ISCCP, and the limits of instrument
902 simluators, *J. Climate*, doi:10.1175/JCLI-D-11-00267.1, in press.
903 Redemann, J., Q. Zhang, P. B. Russell, and J. M. Livingston (2009), Case studies of aerosol
904 remote sensing in the vicinity of clouds, *J. Geophys. Res.*, *114*, D06209,
905 doi:10.1029/2008JD010774.
906 Rogers, R. R., C. A. Hostetler, J. W. Hair, R. A. Ferrare, Z. Liu, M. D. Obland, D. B.
907 Harper, A. L. Cook, K. A. Powell, M. A. Vaughan, and D. M. Winker (2011),

908 Assessment of the CALIPSO Lidar 532 nm attenuated backscatter calibration using the
909 NASA LaRC airborne High Spectral Resolution Lidar, *Atmos. Chem. Phys., 11*, 1,295-
910 1,311, doi:10.5194/acp-11-1295-2011.
911 Romps, D.M, and Z. Kuang (2010), Nature versus nurture in shallow convection, *J. Atmos.*
912 *Sci., 67*, 1655-1666.
913 Rossow, W. B., and R. A. Schiffer (1999), Advances in Understanding Clouds From
914 ISCCP, *Bull. Am. Meteorol. Soc., 80(11)*, 2,261-2,287.
915 Rossow, W.B., C. Delo, and B. Cairns (2002), Implications of the observed mesoscale
916 variations of clouds for the Earth's radiation budget, *J. Climate, 15*, 557-585.
917 Sengupta, S. K., R. M. Welch, M. S. Navar, T. A. Berendes, and D. W. Chen (1990),
918 Cumulus Cloud Field Morphology and Spatial Patterns Derived from High Spatial
919 Resolution Landsat Imagery, *J. App. Meteor., 29*, 1,245-1,267.
920 Siebesma, A. P., C. S. Bretherton, A. Brown, A. Chlond, J. Cuxart, P. G. Duynkerke, H.
921 Jiang, M. Khairoutdinov, D. L., Lewellen, C-H. Moeng, E. Sanchez, B. Stevens, and D.
922 E. Stevens (2003), A Large Eddy Simulation Intercomparison Study of Shallow
923 Cumulus Convection, *J. Atmos. Sci., 60(10)*, 1,201-1,219.
924 Smirnov, A., B. N. Holben, Y. J. Kaufman, O. Dubovik, T. F. Eck, I. Slutsker, C. Pietras,
925 and R. N. Halthore (2002), Optical Properties of Atmospheric Aerosol in Maritime
926 Environments, *J. Atmos. Sci., 59*, 501-523.
927 Stephens. G. L. (1994), Remote Sensing of the Lower Atmosphere. Oxford University
928 Press, 523 pp.
929 Su, W., G. L. Schuster, N. G. Loeb, R. R. Rogers, R. A. Ferrare, C. A. Hostetler, J. W. Hair,
930 and Michael D. Obland (2008), Aerosol and cloud interactions observed from high
931 spectral resolution lidar data, *J. Geophys. Res., 113*, D24202,
932 doi:10.1029/2008JD010588.
933 Tackett, J. L, and L. Di Girolamo (2009), Enhanced aerosol backscatter adjacent to tropical
934 trade wind clouds revealed by satellite-based lidar, *Geophys. Res. Lett., 36*, L14804,
935 doi:10.1029/2009GL039264.
936 Turner, D. D, A. M. Vogelmann, R. T. Austin, J. C. Barnard, K. Dacy-Pereira, J. C. Chiu, S.
937 A. Clough, C. Flynn, M. M. Kahiyer, J. Liljegren, K. Johnson, B. Lin, C. Long, A.
938 Marshak, S. Y. Matrosov, S. A. McFarlane, M. Miller, Q. Min, P. Minnis, W. O'Hirok,
939 Z. Want, and W. Wiscombe (2007), Thin Liquid Water Clouds – Their importance and
940 our challenge, *Bull. Am. Meteorol. Soc., 88(2)*, 177-190, doi:10.1175/BAMS-88-2-177.
941 Twohy, C. H., J. A. Coakley Jr., and W. R. Tahnk (2009), Effect of changes in relative
942 humidity on aerosol scattering near clouds, *J. Geophys. Res., 114*, D05205,
943 doi:1029/2008JD010991.
944 Várnai, T, and A. Marshak (2009), MODIS observations of enhanced clear sky reflectance
945 near clouds, *Geophys. Res. Lett., 36*, L06807, doi:10.1029/2008GL037089.
946 Várnai, T, and A. Marshak (2011), Global CALIPSO Observations of Aerosol Changes
947 Near Clouds, *IEEE Geosci. Remote Sens. Lett., 8(1)*, 19-23.
948 Vaughan, M. A., D. M. Winker, and K. A. Powell (2005), Part 2:Feature Detection and
949 Layer Properties Algorithms. CALIOP Algorithm Theoretical Basis Document PC-
950 SCI-202.01, 87 pp. [Available online at http://www-
951 calipso.larc.nasa.gov/resources/pdfs/PC-SCI-202_Part2_rev1x01.pdf].
952 Vaughan, M. A., K. A. Powell, R. E. Kuehn, S. A. Young, D. M. Winker, C. A. Hostetler,
953 W. H. Hunt, Z. Liu, M. J. McGill, and B. J. Getzewich (2009), Fully Automated
954 Detection of Cloud and Aerosol Layers in the CALIPSO Lidar Measurements, *J. Atmos.*
955 *Oceanic Technol., 26*, 2,034-2,050, doi: 10.1175/2009JTECHA1228.1.

956 Wen, G., A. Marshak, R. E. Cahalan, L. A. Remer, and R. G. Gleidman (2007), 3-D
957 aerosol-cloud radiative interaction observed in collocated MODIS and ASTER images
958 of cumulus cloud fields, *J. Geophys. Res.*, *112*, D13204, doi:10.1029/2006JD008267.
959 Wielicki, B. A., and R. M. Welch (1986), Cumulus Cloud Properties Derived Using Landsat
960 Satellite Data, *J. Clim. Appl, Meteorol.*, *25*, 261-276.
961 Winker, D. M., M. A. Vaughan, A. Omar, Y. Hu, K. A. Powell, Z. Liu, W. H. Hunt, and S.
962 A. Young (2009), Overview of the CALIPSO Mission and CALIOP Data Processing
963 Algorithms, *J. Atmos. Oceanic Technol.*, *26*, 2310–2323, doi:
964 10.1175/2009JTECHA1281.1.
965 Winker, D. M., J. Pelon, J. A. Coakley, S. A. Ackerman, R. J. Charlson, P. R. Colarco, P.
966 Flamant, Q. Fu, R. M. Hoff, C. Kittaka, T. L. Kubar, H. Le Treut, M. P. McCormick, G.
967 Megie, L. Poole, K. Powell, C. Trepte, M. A. Vaughan, and B. A. Wielicki (2010), THE
968 CALIPSO MISSION: A Global View of Aerosols and Clouds, *Bull. Am. Meteorol. Soc.*,
969 *91*, 1,2111-1,220, doi:10.1175/2010BAMS3009.1.
970 Wood. R., and J. P. Taylor (2001), Liquid water path variability in unbroken marine
971 stratocumulus cloud, *Quart. J. Roy. Meteor. Soc.*, *127*, 2,635-2,662.
972 Wood, R., and C. S. Bretherton (2004), Boundary layer Depth, Entrainment, and
973 Decoupling in the Cloud-Capped Subtropical and Tropical marine Boundary Layer, *J.*
974 *Climate*, *17*, 3,576-3,588.
975 Wood, R., and D. L. Hartmann (2006), Spatial Variability of Liquid Water Path in Marine
976 Low Cloud: The Importance of Mesoscale Cellular Convection, *J. Climate*, *19*, 1,748-
977 1,764.
978 Wood, R., and P. R. Field (2011), The Distribution of Cloud Horizontal Sizes, *J. Climate*,
979 *24*, 4,800-4,816, doi:10.1175/2011JCLI4056.1.
980 Wood, R. (2011) Stratocumulus Clouds, *Mon. Wea. Rev.*, doi:10.1175/MWR-D-11-
981 00121.1, in press.
982 Wyant, M. C., C. S. Bretherton, H. A. Rand, and D. E. Stevens (1997) Numerical
983 Simulations and a Conceptual Model of the Stratocumulus to Trade Cumulus Transition,
984 *J. Atmos. Sci.*, *54*, 168–192.
985 Zhang, J., and J. S. Reid (2005), An analysis of potential cloud artifacts in MODIS over
986 ocean aerosol optical thickness products, *Geophys. Res. Lett.*, *32*, L15803,
987 doi:10.1029/2005GL023254.
988 Zhao, G., and L. Di Girolamo (2006), Cloud fraction errors for trade wind cumuli from
989 EOS-Terra instruments, *Geophys. Res. Lett.*, *33*, L20802, doi:10.1029/2006GL028088.
990 Zhao, G., and L. Di Girolamo (2007), Statistics on the macrophysical properties of trade
991 wind cumuli over the tropical western Atlantic, *J. Geophys. Res.*, *112*, D10204,
992 doi:10.1029/2006JD007371.
993 Zuidema, P., D. Leon, A. Pazmany, and M. Cadeddu (2012), Aircraft millimeter-wave
994 passive sensing of cloud liquid water and water vapor during VOCALS-REx, *Atmos.*
995 *Chem. Phy.*, *12*, 355-369, doi:10.5194/acp-12-355-2012.
996

TABLES

Table 1. CALIOP – HSRL matched dataset description. [a]

Date	Location[b]	Overpass Time[c]	Cloud Type[d]
26 Jan 2007	36.88°N, 75.52°W	07:11	-
23 May 2007	32.41°N, 77.07°W	18:32	Cumulus
26 Jan 2008	12.43°N, 60.26°W	17:36	Cumulus
11 Aug 2010	33.59N, 65.09W	17:43	Cumulus/Stratocumulus
18 Aug 2010	22.38°N, 63.95°W	17:48	Cumulus
22 Aug 2010	13.71°N, 69.04°W	06:39	-
24 Aug 2010	21.76°N, 64.09°W	06:15	-
26 Aug 2010	20.67N, 61.25W	06:02	-

[a] Transect lengths range from 34 km to 215 km, with an 8-day mean of 126 km.
[b] Segment mid-point (latitude, longitude).
[c] Times are UTC.
[d] Cloud type information from inspection of MODIS Aqua L1B Granule Images (daytime only), (http://modis-atmos.gsfc.nasa.gov/IMAGES/index_myd021km.html).

Table 2. Cloud cover[a] definitions for this work.

Parameter[b]	Definition	Equation[c]
Low-cloud cover (f_{cld})	The fraction of all high-cloud-screened clear and cloud profiles within a gridbox that are clouds.	$\sum N_{cloud} \Big/ \sum (N_{clear} + N_{cloud})$
Optically-thin low-cloud cover (f_{thin})	The fraction of all high-cloud-screened clear and cloud profiles within a gridbox that are optically-thin.	$\sum N_{thin} \Big/ \sum (N_{clear} + N_{cloud})$
Optically-thin fraction of low-cloud ($f_{thin,cld}$) i.e. $f_{thin}/f_{cld} = f_{thin,cld}$	The fraction of high-cloud-screened cloud profiles within a gridbox that are optically-thin.	$\sum N_{thin} \Big/ \sum N_{cloud}$

[a] Unless otherwise stated, all gridbox cloud cover values are two-year averages of monthly calculated values.

[b] All parameters are calculated at full-resolution.

[c] N is the number of full-resolution profiles within a gridbox that are: cloudy (N_{cloud}), cloudy and optically-thin (N_{thin}), clear (N_{clear}).

1013 **Table 3.** Stratocumulus (Sc), Cumulus (Cu), and transition from Sc to Cu regime
1014 (Sc-Cu), region details: location, low-cloud cover (f_{cld}), optically-thin fraction of
1015 low-cloud ($f_{cld,thin}$).

Cloud Type	Latitude	Longitude	f_{cld} [a,b]	$f_{thin,cld}$ [a,b]
Sc	20°N - 30°N	120°W - 130°W	0.79	0.36
Sc-Cu	10°N - 15°N	130°W - 140°W	0.70	0.37
Cu	10°S - 20°S	150°W - 160°W	0.26	0.84

1016 [a] f_{cld} and $f_{cld,thin}$ are two-year means of monthly values. N = 96 (24 months x 4 gridbox values)
1017 [b] f_{cld} and $f_{cld,thin}$ sampling uncertainties are 0.02 – 0.04 (95% confidence level), and are estimated from the
1018 bootstrap method [*Efron and Gong*, 1983].
1019

Table 4. Cumulus cloud-field observed and modeled parameters.

Instrument	f_{cld}	$f_{thin,cld}$	β[a]	α_{TOA}[b]
Observed:				
CALIOP	0.26(0.11)[c]	0.84(0.13)[c]	2.66±0.43	
CERES				0.16
MODIS				0.11
Model[d]				
CALIOP	0.24	0.81	2.69±0.51	0.14
HSRL	0.24	0.83	2.46±0.29	-
HSRL full-res[e]	0.12	0.86	2.74±0.42	-
MODIS	0.17	0.60	2.12±0.70	-

[a] Cloud length distribution power law exponent±95% CI.

[b] Top-of-atmosphere albedo (α_{TOA}) values are used to constrain model mean (clear and cloudy) optical depth. CERES shortwave TOA albedo (*http://eos.atmos.washington.edu/cgi-bin/ceres/disp.pl?ceres.alb.ann.d*) and MODIS reflectance (R_{MODIS}) estimated as $R_{MODIS} = R_{cld}\, f_{cld} + R_{clr}\, f_{clr}$, where R_{cld} is mean visible cloud reflectance [*Wood and Field*, 2011] at 1 km cloud length (minimum observable MODIS cloud length), R_{clr} is a typical visible clear-sky reflectance (0.08), and f_{cld},and f_{clr} weights are CALIOP observed cloud and clear fractions, for the tropical Pacific trade wind cumulus region [15°S, 155°W; center latitude, longitude]. We estimate model TOA albedo using model τ_{cld} and a simplified cloud albedo equation based upon a two-stream approximation and assumed asymmetry parameter of 0.85 ($\alpha^{cld} \approx \tau_{cld} / \tau_{cld} + 7.7$) [*Lacis and Hansen*, 1974]. Cloud albedo is calculated for every data point with τ_{cld} greater than 0.03 in the modeled cloud field, and these data are input to a simple TOA albedo model ($\alpha^{TOA} = R_{clr} + [(1 - R_{clr})^2 * (R_{cld} + R^*_{cld})/1 - R_{clf} * (R_{cld} + R^*_{cld})]$, where $R^*_{cld} = R_{sfc} * [(1 - R_{cld})^2/1-(R_{cld} * R_{sfc})]$, with assumed ocean surface albedo (R_{sfc}) of 0.05.

[c] CALIOP two-year cloud cover mean (standard deviation) of monthly values. N = 96 (24 months x 4 gridbox values).

[d] Cloud Optical depth (τ_{cld}) threshold for CALIOP and HSRL is τ greater than 0.03 and for MODIS is τ greater than 0.4 [*Ackerman et al*., 2008]. Optically-thin τ_{cld} threshold is τ_{cld} less than or equal to 3 [*Winker et al*., 2010] for all simulated instrument FOVs sampling of model output.

[e] Highest resolution HSRL achieved given the HSRL PRF = 200 Hz and assuming aircraft velocity = 120 m s^{-1} (0.6 m).

1041 **FIGURE CAPTIONS**

1042 **Figure 1.** Cumulative fraction of MODIS L3 liquid water cloud optical depth (τ_{cld}) for 12
1043 months of ocean daytime data spanning ±45° latitude. Cloud albedo is approximated as
1044 (τ_{cld}/τ_{cld}+7.7) [*Lacis and Hansen*, 1974]. MODIS data suggest approximately one-third of
1045 low-clouds over the oceans have optical depth less than 3 (optically-thin cloud definition,
1046 this study). In addition, such clouds may contribute up to 15% to total low-cloud albedo.
1047 Inset figure describes relative scales of CALIOP receiver footprint at single-shot resolution
1048 and MODIS pixel at cloud product resolution. It should be noted that at most, 3 CALIPSO
1049 footprints will traverse a given MODIS (on Aqua) pixel.
1050

1051 **Figure 2.** a) A bimodal distribution of 2 years of ocean nighttime lidar integrated attenuated
1052 backscatter signal at 532 nm (integrated from 0 to 3 km altitude), red dashed line is
1053 Rayleigh IABS from CALIOP molecular number density profile for a tropical Pacific
1054 transect. The modes represent clear and cloudy atmospheric regions, as classified by the
1055 CALIOP Vertical Feature Mask cloud-aerosol discrimination algorithm; b) marine low-
1056 cloud data suggests optically-thin cloud profiles (as defined in Section 2) populate not only
1057 the clear-cloud transition region, but also the broader marine low-cloud field.
1058

1059 **Figure 3**. a) A two-dimensional (5 km x 10 km), and, b) one-dimensional (10 km) view of a
1060 high-cloud-screened broken marine low-cloud scene, generated from CALIOP data along a
1061 10 km daytime orbit segment over the northwest tropical Atlantic [32°N, 77°W] on 27 May
1062 2007: a) Wide Field Camera (WFC) band-averaged radiance (620-670 nm) at 125 m
1063 horizontal resolution with CALIOP ground track position superimposed. The WFC data are
1064 continuous, along-track radiances. Symbols along the CALOP track indicate clear (yellow
1065 square), optically-thin cloud (white circle), and optically-thick cloud (black circle), b)
1066 Collocated WFC radiance (black) and Level 1 532 nm attenuated backscatter integrated
1067 from 0 to 20 km (IABS) (pink) for the same segment as in a). Symbols identifying clear
1068 profiles, and cloud profiles flagged as optically-thin or optically-thick are also indicated in
1069 b).
1070

Figure 4. Number of data points comprising a) the primary dataset for this analysis, i.e., the high-cloud-screened non-polar ocean dataset, and b) the high-cloud-screened cloud length dataset Data for cloud length calculations are a subset of a), requiring a continuous transect at least 100 km in length. Data are 5° x 5° resolution. Total number of data points: a) 1.4 x 10^8, b) 3.9 x 10^7.

Figure 5. Two-year mean ocean nighttime a) marine low-cloud cover, b) optically-thin marine low-cloud cover, and c) optically-thin fraction of marine low-cloud (see Table 2 for fraction definitions). Data are 5°x5° resolution. Corresponding domain-averaged values are a) 0.50 (0.25), b) 0.23 (0.09), and c) 0.45 (0.28), mean (standard deviation). For this calculation gridbox values are weighted by the fraction of each gridbox that is ocean, and f_{thin_cld} *values are also weighted by* f_{cld}.

Figure 6. Joint distribution of monthly nighttime gridded optically-thin fraction of marine low-cloud, as function of marine low-cloud cover, over-plotted with two-year mean gridbox values (grey). Both monthly and two-year averaged data exhibit a strong negative correlation. The correlation coefficient for the monthly data is -0.83, significant at the 95% confidence level.

Figure 7. Cloud length distribution based upon two years of gridded data for marine low-cloud, "majority optically-thin" cloud, and "majority optically-thick" cloud. Each "Majority" category includes only clouds comprising greater than 90% cloud profiles belonging to either the optically-thin or optically-thick category. Size bins are logarithmically spaced and ordinate axis is normalized frequency. $\beta = 2$ line shown for reference. Inset: marine low-cloud length distribution for the following regions [region center latitude, longitude]: California stratocumulus region (Sc) [25°N, 125°W], tropical Pacific stratocumulus to cumulus transition (Sc-Cu Trans) [15°N, 135°W], and tropical Pacific trade wind cumulus (Cu) [15°S, 155°W]. Abscissa values are cloud length bin centers.

Figure 8. Cloud length at median cloud cover (L_{50}) for a) marine low-cloud, b) "majority optically-thin" cloud, c) "majority optically-thick" cloud, from two years of ocean nighttime data at 5°x5° resolution. Low (high) cloud cover values are dominated by small (large) clouds. "Majority optically-thin" clouds dominate the cloud type in regions of low cloud cover, e.g. trade wind cumulus regions. Each "majority" category includes only clouds comprising greater than 90% cloud profiles belonging to either the optically-thin or optically-thick category. White over ocean regions in c) indicates that no "majority optically-thick" clouds observed.

Figure 9. HSRL (black) and CALIOP (pink) marine low-cloud length distributions with bootstrap derived 95% confidence intervals (CI) [*Efron and Gong,* 1983]. Dashed line is $\beta = 2$, shown for reference. HSRL samples more clouds at smaller sizes than CALIOP. Sub-sampling HSRL (blue stars) produces good agreement between HSRL and CALIOP size distributions. CALIOP and HSRL mean f_{cld} values agree to within 2 standard deviations. However, mean $f_{thin,cld}$ values do not agree, with HSRL $f_{thin,cld}$ lower than CALIOP $f_{thin,cld}$. Inset schematic describes suggested mechanism for $f_{thin,cld}$ discrepancy, i.e., it is the result of differences in instrument sampling methods: blue circles represent CALIOP 90 m FOVs, and orange bar shows the relative size of the HSRL FOV compared to the CALIOP FOV. .

Figure 10. Optically-thin fraction of marine low-cloud length for non-polar oceans, and three regions with different dominant cloud types [region center latitude, longitude]: California stratocumulus region (Sc) [25°N, 125°W], tropical Pacific stratocumulus to cumulus transition (Sc-Cu Trans) [15°N, 135°W], and tropical Pacific trade wind cumulus (Cu) [15°S, 155°W]. Increasing optically-thin fraction as cloud length decreases is observed across all regions, despite different cloud types. Vertical bars are 95% confidence intervals calculated from the bootstrap method [*Efron and Gong,* 1983]. Abscissa values are cloud length bin centers.

Figure 11. Vertical distribution of two-year mean optically-thick (red) and optically-thin (black) cloud top height (top row) and, optically-thin cloud base height (bottom row) for 3 cloud regimes [region center latitude, longitude]: a) and d) California stratocumulus region

(Sc) [25°N, 125°W], b) and e) tropical Pacific stratocumulus to cumulus transition (Sc-Cu Trans) [15°N, 135°W], and c) and f) tropical Pacific trade wind cumulus (Cu) [15°S, 155°W]. Layer boundaries are identified by CALIPSO feature detection algorithm at full horizontal resolution, and 60m vertical resolution.

Figure 12. Normalized density distributions of optically-thin cloud top height and layer depth for 3 cloud types [region center latitude, longitude]: a) California stratocumulus region [25°N, 125°W], b) tropical Pacific stratocumulus to cumulus transition (Sc-Cu Trans) [15°N, 135°W], and c) tropical Pacific trade wind cumulus (Cu) [15°S, 155°W]. Inset figures are layer depth distributions for each region, overlaid with a gamma distribution (red). Text is region mean (standard deviation) layer depth (km), and number of full-resolution optically-thin cloud profiles for each region. Layer depth histogram is normalized such that the area under the curve = 1.

Figure 13. An aerial photograph of a typical trade wind cumulus cloud field observed in the Western Caribbean during the Rain in Cumulus over Ocean (RICO) field program. Apparent is the wide range of cloud depths and horizontal extents. (Image courtesy of B. Stevens).

Figure 14. Two years of CALIOP tropical Pacific trade wind region observations (black dots) ± 95% confidence intervals from bootstrap method [*Efron and Gong*, 1983], and cascade model output simulating this cloud regime, sampled with CALIOP FOV (black circles), MODIS FOV (red circles), HSRL FOV (blue circles), and HSRL Full Res i.e., highest resolution sampling of model output (blue squares). Size bins are logarithmically spaced and ordinate axis is normalized frequency. $\beta = 2$ line (dashed line) shown for reference. Cascade model output from 100 runs with $H = 0.015$ and $p = 0.05$. Abscissa values are cloud length bin centers.

Figure 15. Cloudy FOVs and partially cloud-filled FOVs (pFOVs) metrics binned by cloud length, as described by model simulated optical depth (τ) values, sampled at CALIOP FOV resolution. Displayed for each cloud length-bin is the fraction of all cloud FOVs that are

1163 less than 100% cloudy, i.e., pFOV (filled circles); the median cloud fraction for pFOVs
1164 (filled squares); the fraction of optically-thin pFOVs incorrectly classified as optically-thin,
1165 i.e., a FOV with mean τ less than or equal to 3 and mean τ of the cloudy-only segment
1166 greater than 3 (filled diamonds); the distribution of the optically-thin fraction of the cloud
1167 segment within a pFOV, where the box notch indicates that median fraction, upper and
1168 lower lines are the upper and lower quartile values, and whiskers are 1.5 x interquartile
1169 range. Cascade model output from 100 runs with H = 0.015 and p = 0.05.
1170

1171

1172

FIGURES

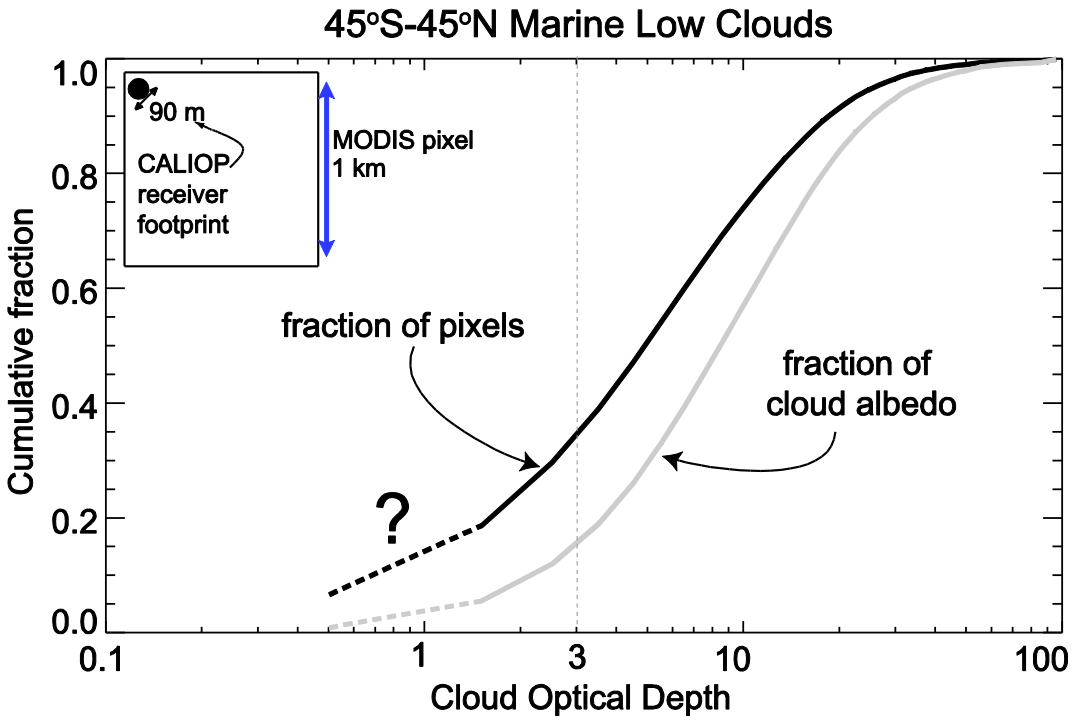

Figure 1. Cumulative fraction of MODIS L3 liquid water cloud optical depth (τ_{cld}) for 12 months of ocean daytime data spanning ±45° latitude. Cloud albedo is approximated as (τ_{cld}/τ_{cld}+7.7) [*Lacis and Hansen*, 1974]. MODIS data suggest approximately one-third of low-clouds over the oceans have optical depth less than 3 (optically-thin cloud definition, this study). In addition, such clouds may contribute up to 15% to total low-cloud albedo. Inset figure describes relative scales of CALIOP receiver footprint at single-shot resolution and MODIS pixel at cloud product resolution. It should be noted that at most, 3 CALIPSO footprints will traverse a given MODIS (on Aqua) pixel.

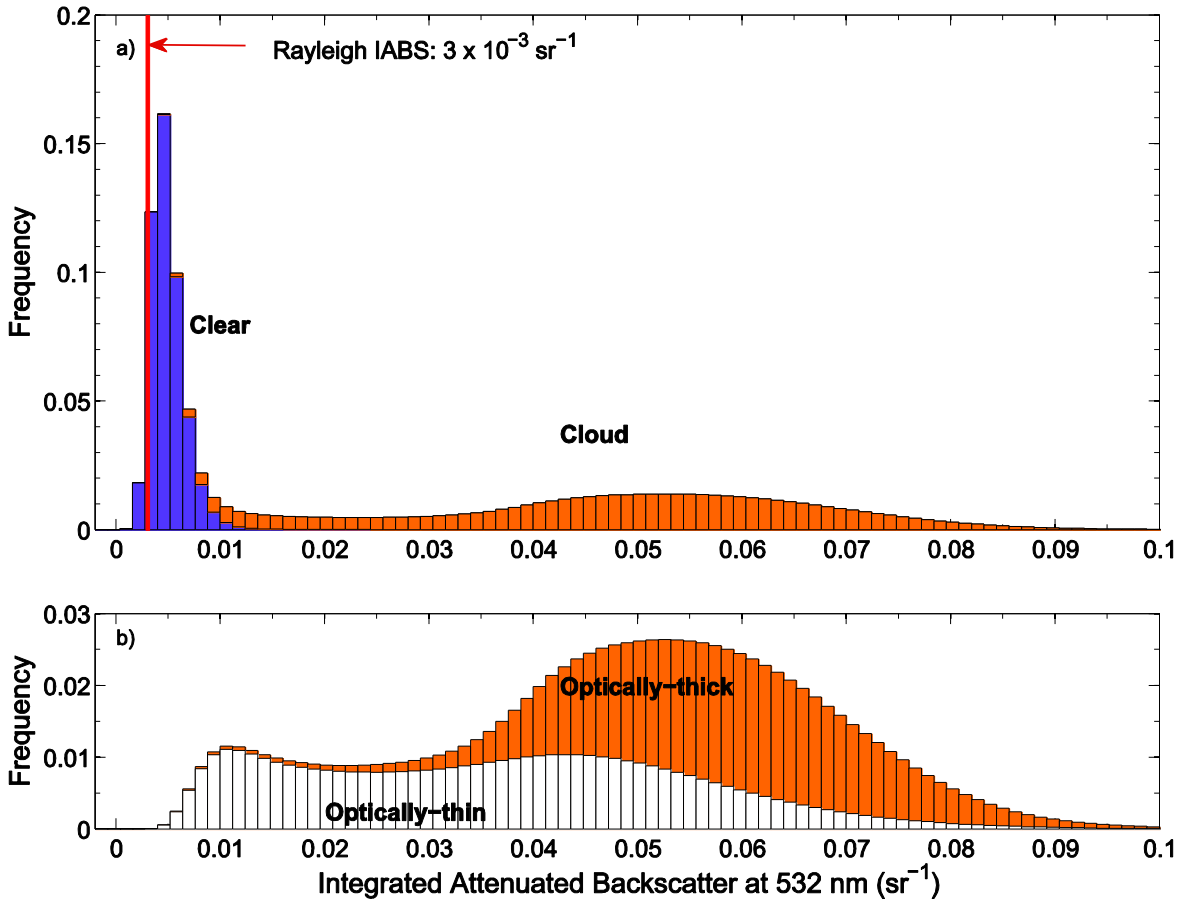

Figure 2. a) A bimodal distribution of 2 years of ocean nighttime lidar integrated attenuated backscatter signal at 532 nm (integrated from 0 to 3 km altitude), red dashed line is Rayleigh IABS from CALIOP molecular number density profile for a tropical Pacific transect. The modes represent clear and cloudy atmospheric regions, as classified by the CALIOP Vertical Feature Mask cloud-aerosol discrimination algorithm; b) marine low-cloud data suggests optically-thin cloud profiles (as defined in Section 2) populate not only the clear-cloud transition region, but also the broader marine low-cloud field.

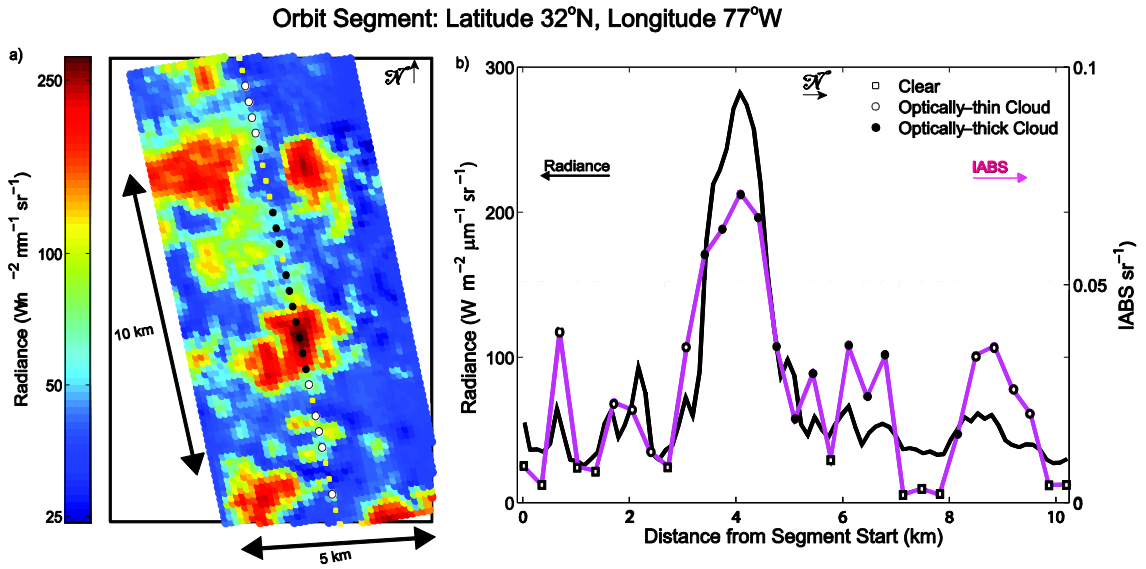

Figure 3. a) A two-dimensional (5 km x 10 km), and, b) one-dimensional (10 km) view of a high-cloud-screened broken marine low-cloud scene, generated from CALIOP data along a 10 km daytime orbit segment over the northwest tropical Atlantic [32°N, 77°W] on 27 May 2007: a) Wide Field Camera (WFC) band-averaged radiance (620-670 nm) at 125 m horizontal resolution with CALIOP ground track position superimposed. The WFC data are continuous, along-track radiances. Symbols along the CALOP track indicate clear (yellow square), optically-thin cloud (white circle), and optically-thick cloud (black circle), b) Collocated WFC radiance (black) and Level 1 532 nm attenuated backscatter integrated from 0 to 20 km (IABS) (pink) for the same segment as in a). Symbols identifying clear profiles, and cloud profiles flagged as optically-thin or optically-thick are also indicated in b).

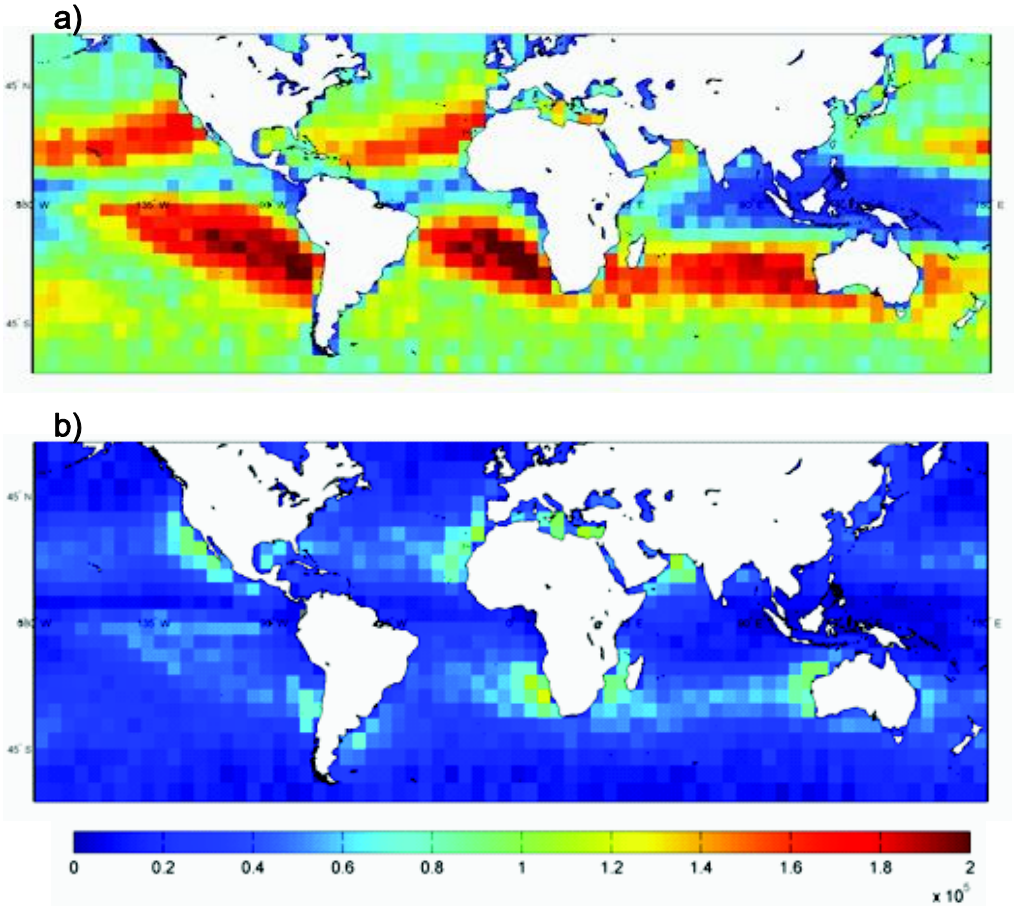

Figure 4. Number of data points comprising a) the primary dataset for this analysis, i.e., the high-cloud-screened non-polar ocean dataset, and b) the high-cloud-screened cloud length dataset Data for cloud length calculations are a subset of a), requiring a continuous transect at least 100 km in length. Data are 5° x 5° resolution. Total number of data points: a) 1.4 x 10^8, b) 3.9 x 10^7.

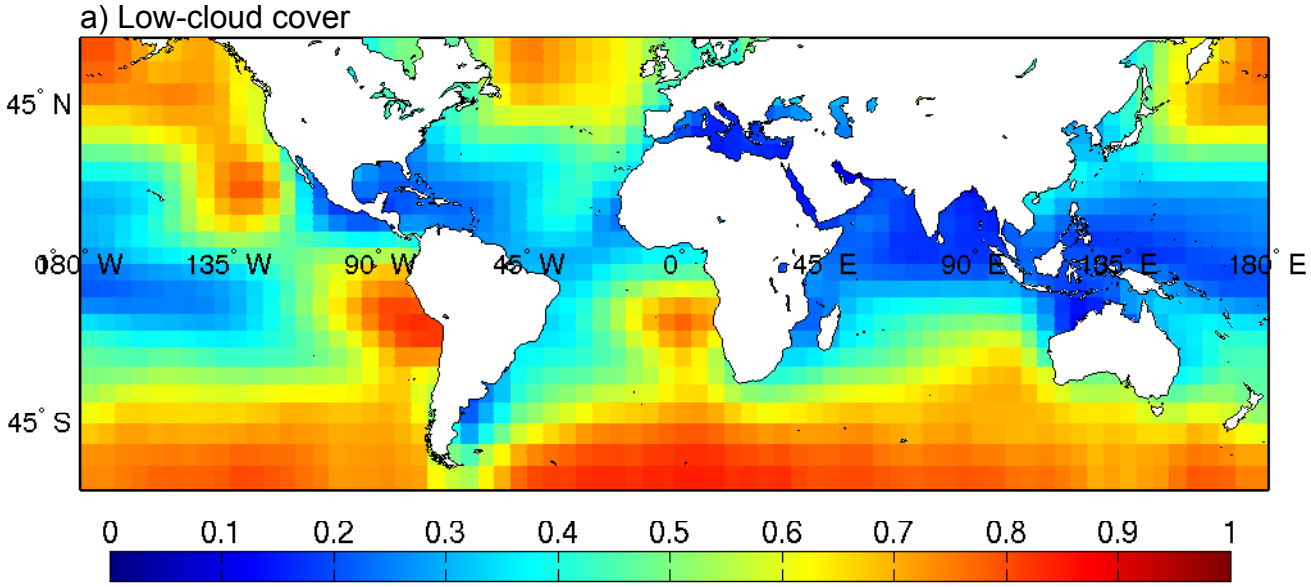
a) Low-cloud cover
45˚ N
45˚ S
180˚ W
135˚ W
90˚ W
45˚ W
0˚
45˚ E
90˚ E
135˚ E
180˚ E
0
0.1
0.2
0.3
0.4
0.5
0.6
0.7
0.8
0.9
1

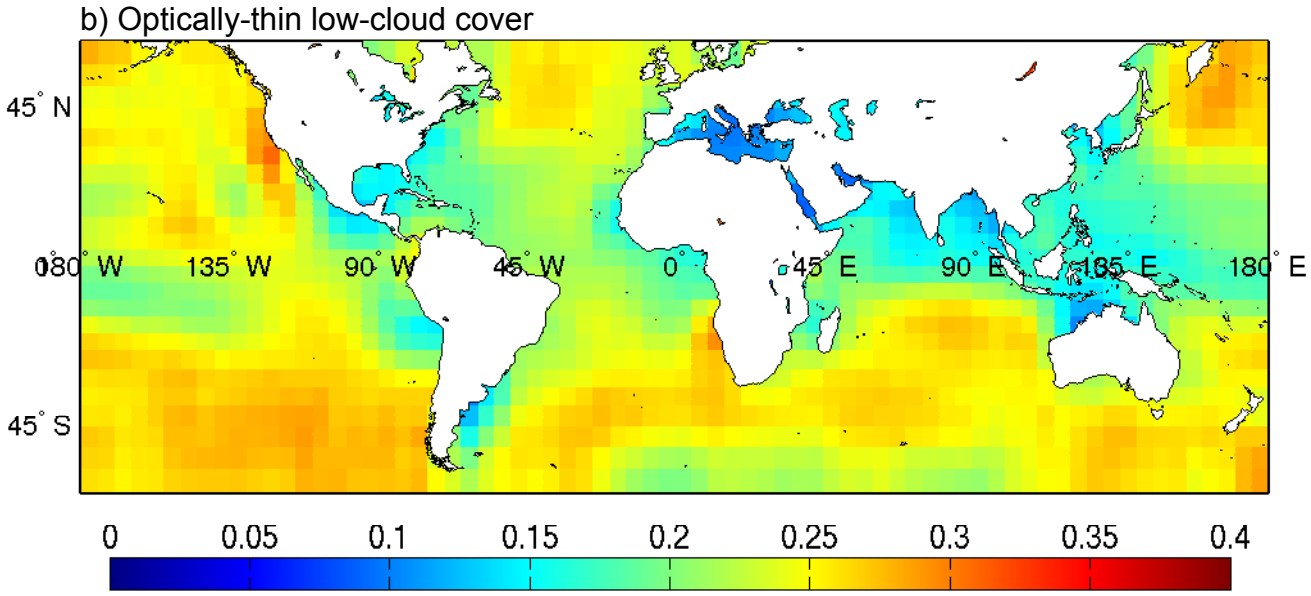
b) Optically-thin low-cloud cover
45˚ N
45˚ S
180˚ W
135˚ W
90˚ W
45˚ W
0˚
45˚ E
90˚ E
135˚ E
180˚ E
0
0.05
0.1
0.15
0.2
0.25
0.3
0.35
0.4

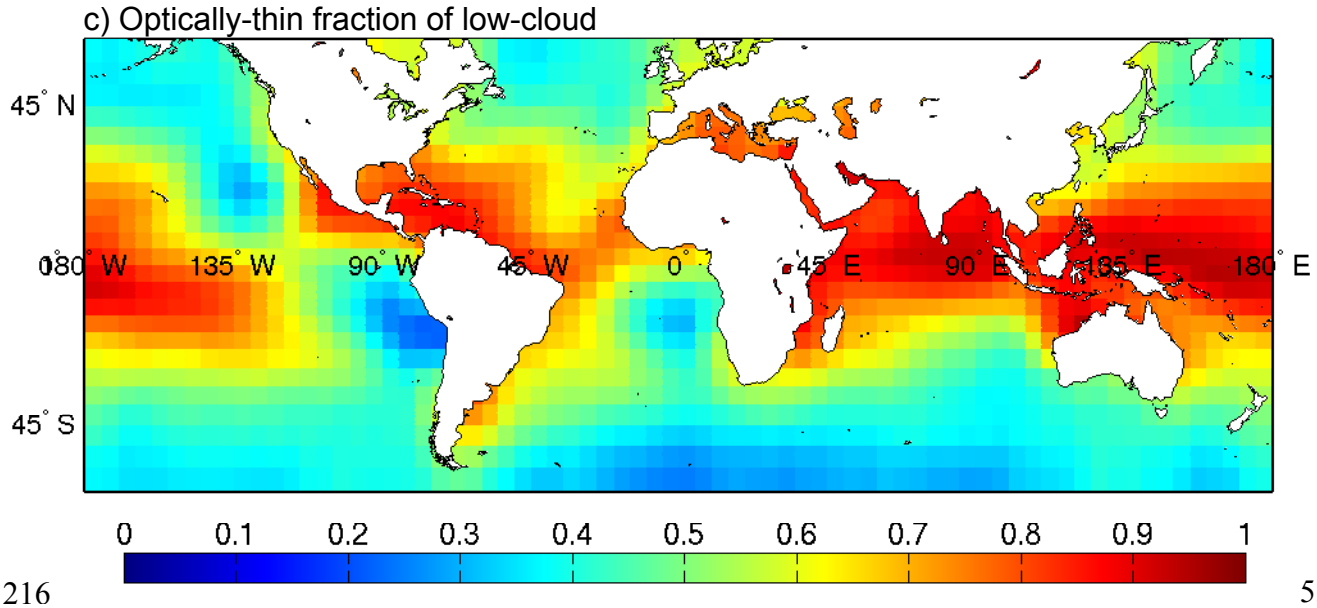
c) Optically-thin fraction of low-cloud
45˚ N
45˚ S
180˚ W
135˚ W
90˚ W
45˚ W
0˚
45˚ E
90˚ E
135˚ E
180˚ E
0
0.1
0.2
0.3
0.4
0.5
0.6
0.7
0.8
0.9
1

Figure 5. Two-year mean ocean nighttime a) marine low-cloud cover, b) optically-thin marine low-cloud cover, and c) optically-thin fraction of marine low-cloud (see Table 2 for fraction definitions). Data are 5°x5° resolution. Corresponding domain-averaged values are a) 0.50 (0.25), b) 0.23 (0.09), and c) 0.45 (0.28), mean (standard deviation). For this calculation gridbox values are weighted by the fraction of each gridbox that is ocean, and f_{thin_cld} values are also weighted by f_{cld}.

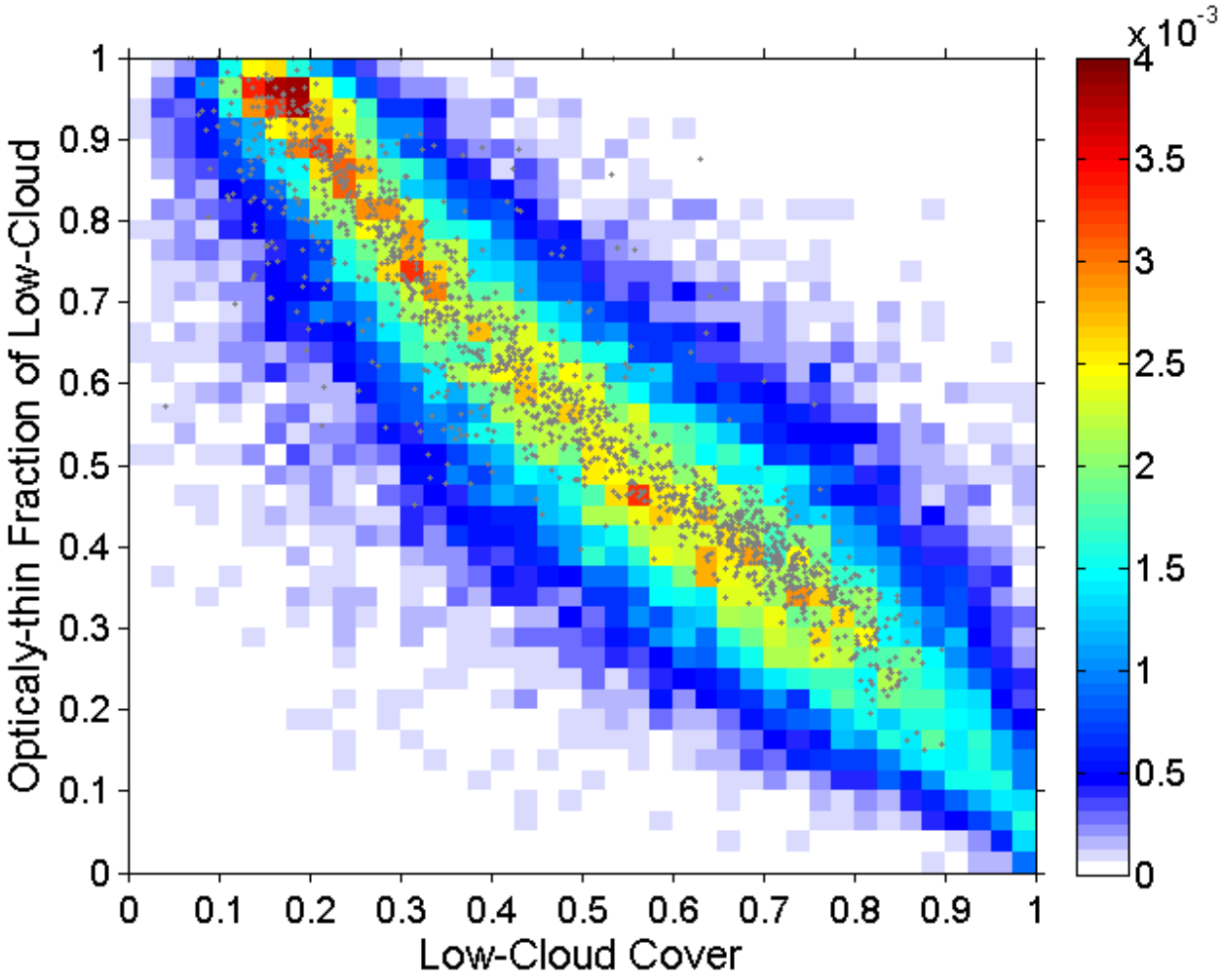

Figure 6. Joint distribution of monthly nighttime gridded optically-thin fraction of marine low-cloud, as function of marine low-cloud cover, over-plotted with two-year mean gridbox values (grey). Both monthly and two-year averaged data exhibit a strong negative correlation. The correlation coefficient for the monthly data is -0.83, significant at the 95% confidence level.

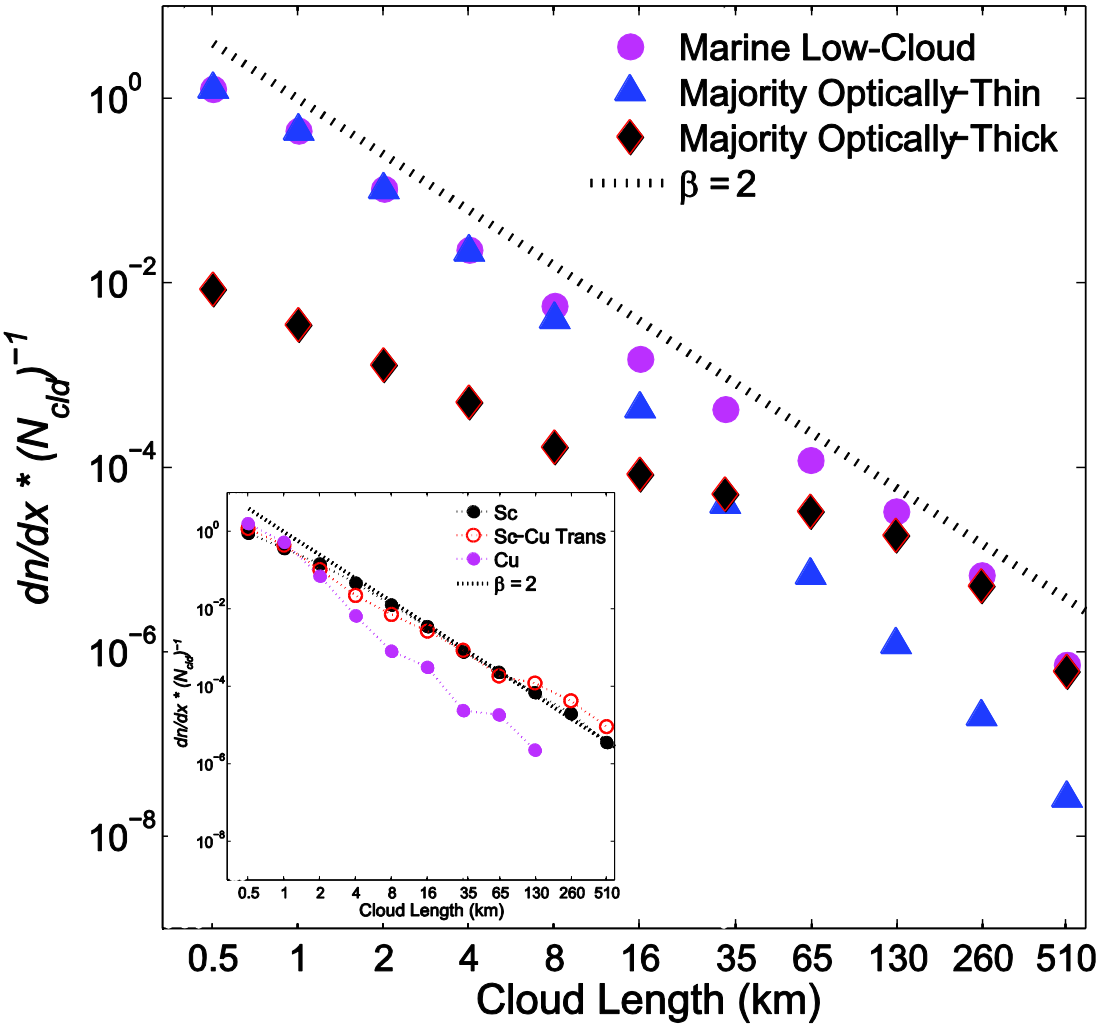

Figure 7. Cloud length distribution based upon two years of gridded data for marine low-cloud, "majority optically-thin" cloud, and "majority optically-thick" cloud. Each "Majority" category includes only clouds comprising greater than 90% cloud profiles belonging to either the optically-thin or optically-thick category. Size bins are logarithmically spaced and ordinate axis is normalized frequency. $\beta = 2$ line shown for reference. Inset: marine low-cloud length distribution for the following regions [region center latitude, longitude]: California stratocumulus region (Sc) [25°N, 125°W], tropical Pacific stratocumulus to cumulus transition (Sc-Cu Trans) [15°N, 135°W], and tropical Pacific trade wind cumulus (Cu) [15°S, 155°W]. Abscissa values are cloud length bin centers.

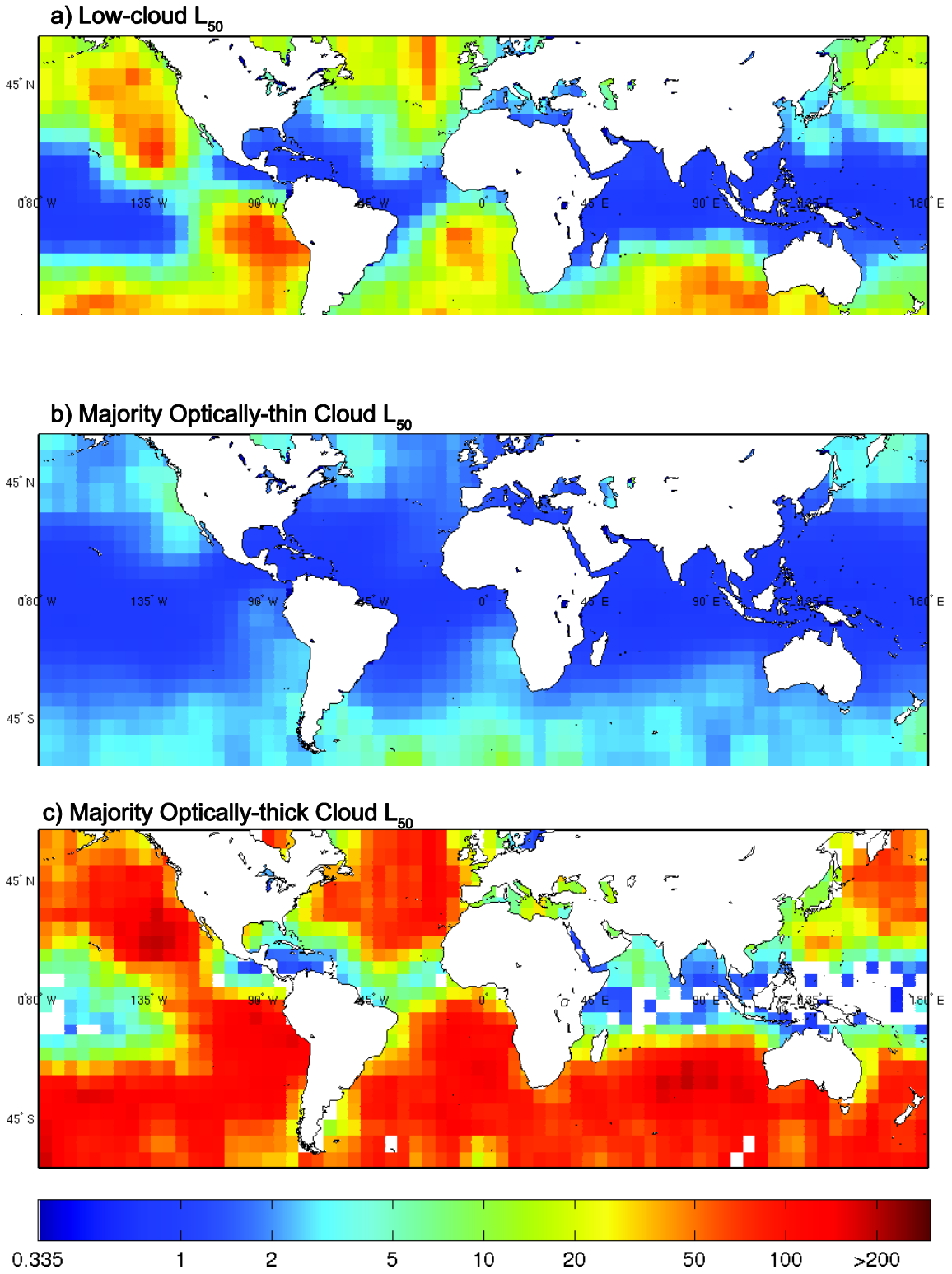

Figure 8. Cloud length at median cloud cover (L_{50}) for a) marine low-cloud, b) "majority optically-thin" cloud, c) "majority optically-thick" cloud, from two years of ocean nighttime data at 5°x5° resolution. Low (high) cloud cover values are dominated by small (large) clouds. "Majority optically-thin" clouds dominate the cloud type in regions of low cloud cover, e.g. trade wind cumulus regions. Each "majority" category includes only clouds

comprising greater than 90% cloud profiles belonging to either the optically-thin or optically-thick category. White over ocean regions in c) indicates that no "majority optically-thick" clouds observed.

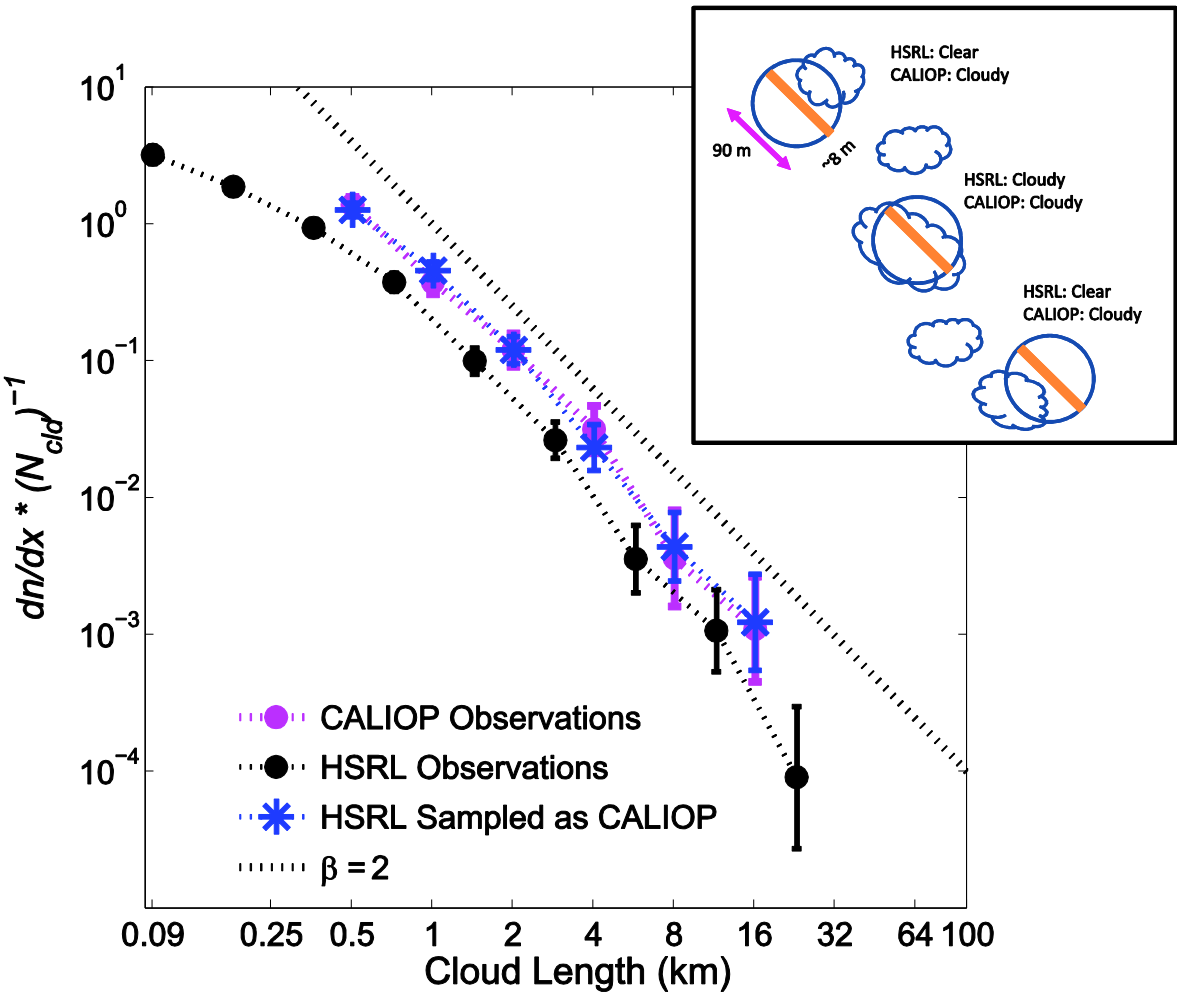

Figure 9. HSRL (black) and CALIOP (pink) marine low-cloud length distributions with bootstrap derived 95% confidence intervals (CI) [*Efron and Gong*, 1983]. Dashed line is $\beta = 2$, shown for reference. HSRL samples more clouds at smaller sizes than CALIOP. Sub-sampling HSRL (blue stars) produces good agreement between HSRL and CALIOP size distributions. CALIOP and HSRL mean f_{cld} values agree to within 2 standard deviations. However, mean $f_{thin,cld}$ values do not agree, with HSRL $f_{thin,cld}$ lower than CALIOP $f_{thin,cld}$. Inset schematic describes suggested mechanism for $f_{thin,cld}$ discrepancy, i.e., it is the result of differences in instrument sampling methods: blue circles represent CALIOP 90 m FOVs, and orange bar shows the relative size of the HSRL FOV compared to the CALIOP FOV. .

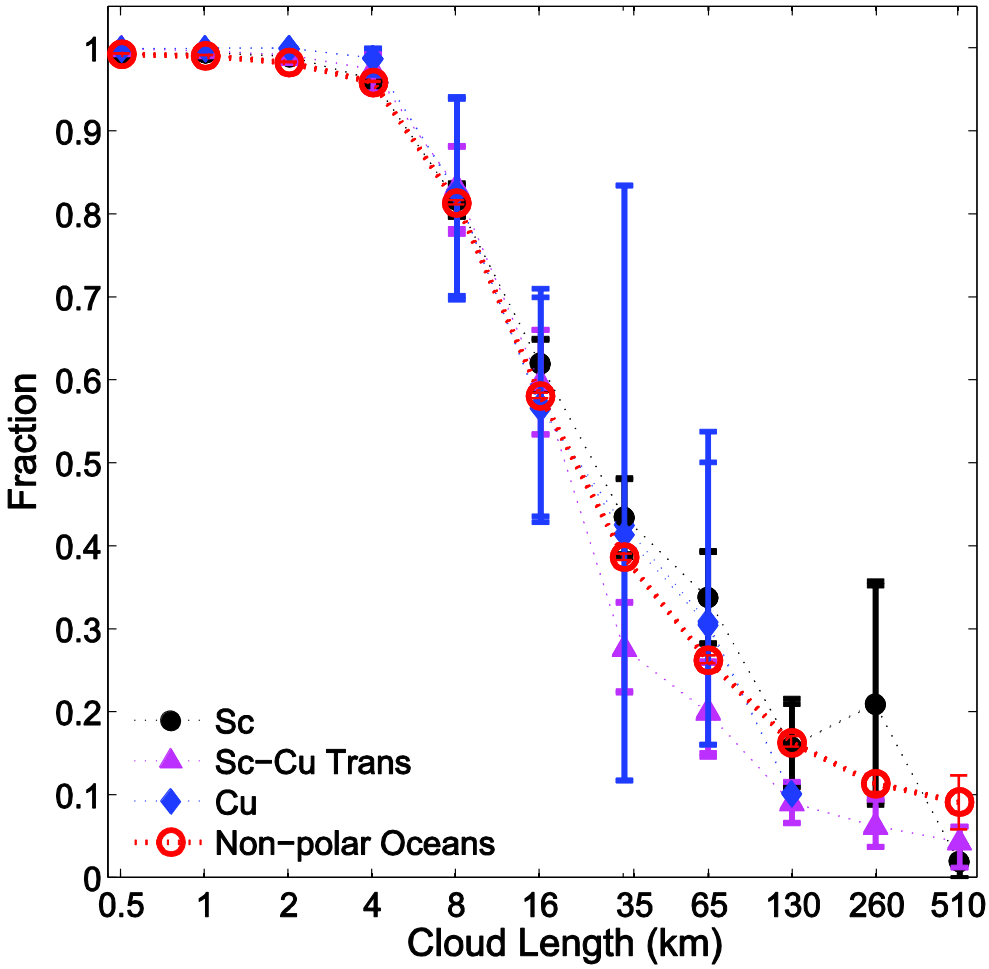

Figure 10. Optically-thin fraction of marine low-cloud length for non-polar oceans, and three regions with different dominant cloud types [region center latitude, longitude]: California stratocumulus region (Sc) [25°N, 125°W], tropical Pacific stratocumulus to cumulus transition (Sc-Cu Trans) [15°N, 135°W], and tropical Pacific trade wind cumulus (Cu) [15°S, 155°W]. Increasing optically-thin fraction as cloud length decreases is observed across all regions, despite different cloud types. Vertical bars are 95% confidence intervals calculated from the bootstrap method [*Efron and Gong*, 1983]. Abscissa values are cloud length bin centers.

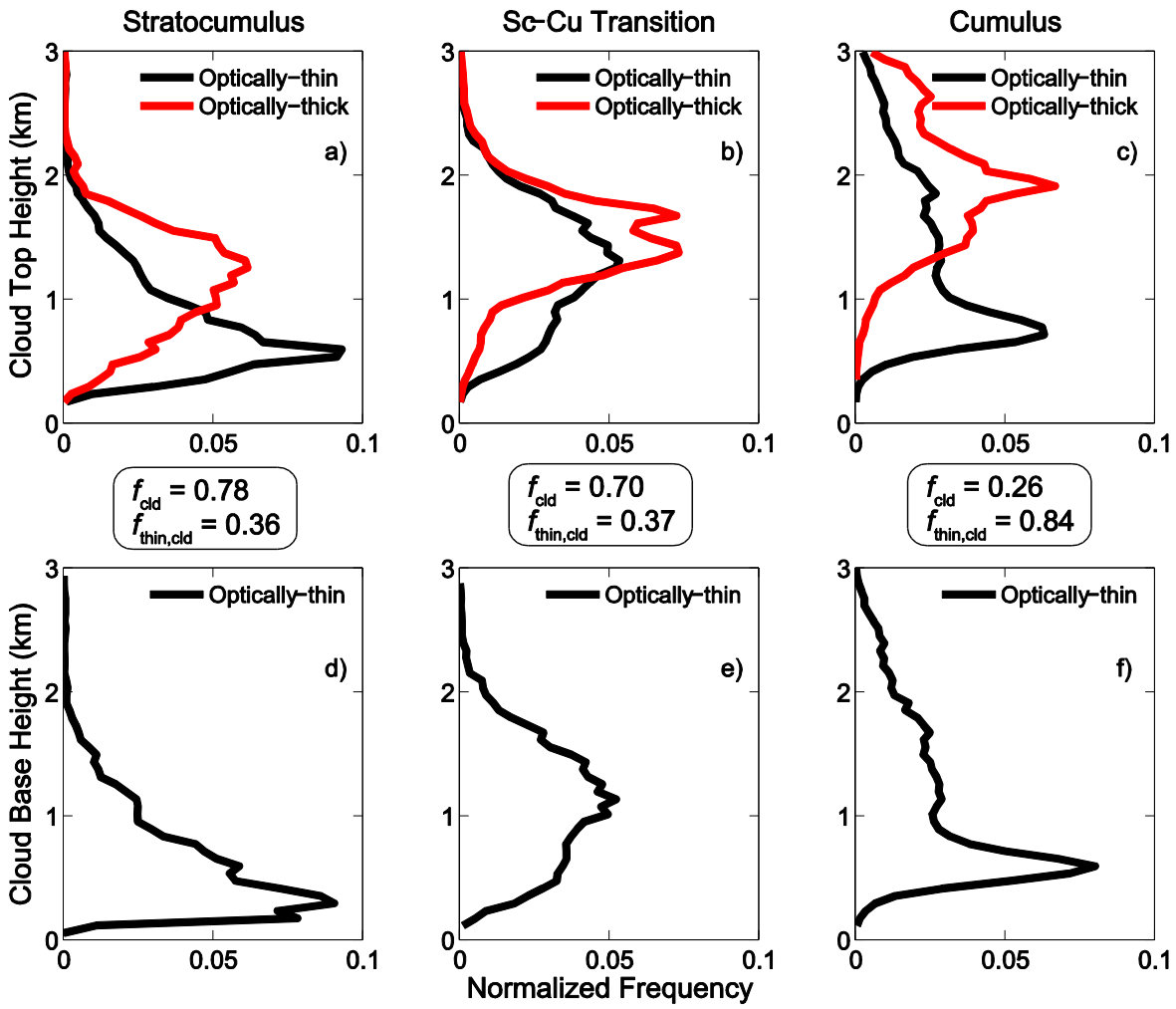

Figure 11. Vertical distribution of two-year mean optically-thick (red) and optically-thin (black) cloud top height (top row) and, optically-thin cloud base height (bottom row) for 3 cloud regimes [region center latitude, longitude]: a) and d) California stratocumulus region (Sc) [25°N, 125°W], b) and e) tropical Pacific stratocumulus to cumulus transition (Sc-Cu Trans) [15°N, 135°W], and c) and f) tropical Pacific trade wind cumulus (Cu) [15°S, 155°W]. Layer boundaries are identified by CALIPSO feature detection algorithm at full horizontal resolution, and 60m vertical resolution.

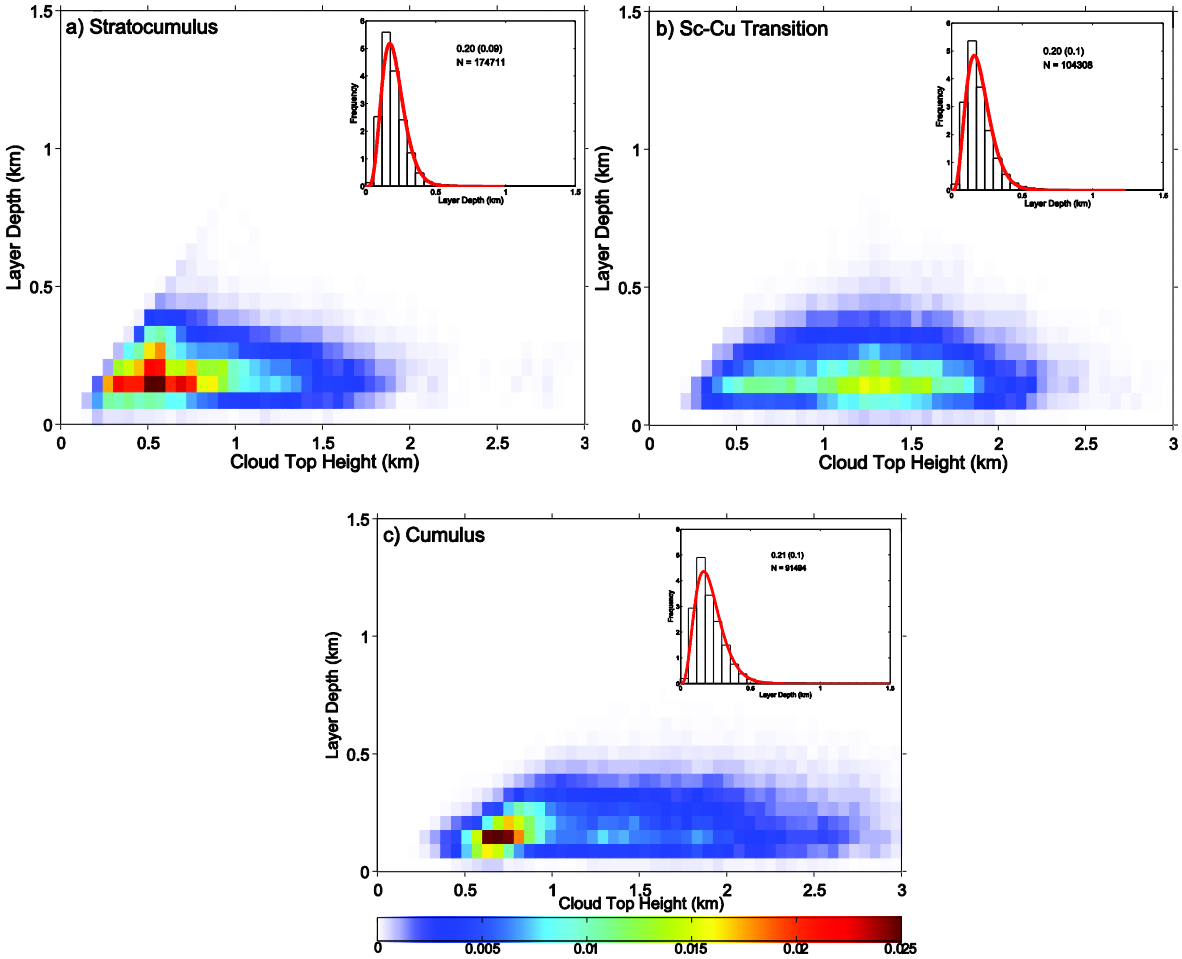

Figure 12. Normalized density distributions of optically-thin cloud top height and layer depth for 3 cloud types [region center latitude, longitude]: a) California stratocumulus region [25°N, 125°W], b) tropical Pacific stratocumulus to cumulus transition (Sc-Cu Trans) [15°N, 135°W], and c) tropical Pacific trade wind cumulus (Cu) [15°S, 155°W]. Inset figures are layer depth distributions for each region, overlaid with a gamma distribution (red). Text is region mean (standard deviation) layer depth (km), and number of full-resolution optically-thin cloud profiles for each region. Layer depth histogram is normalized such that the area under the curve = 1.

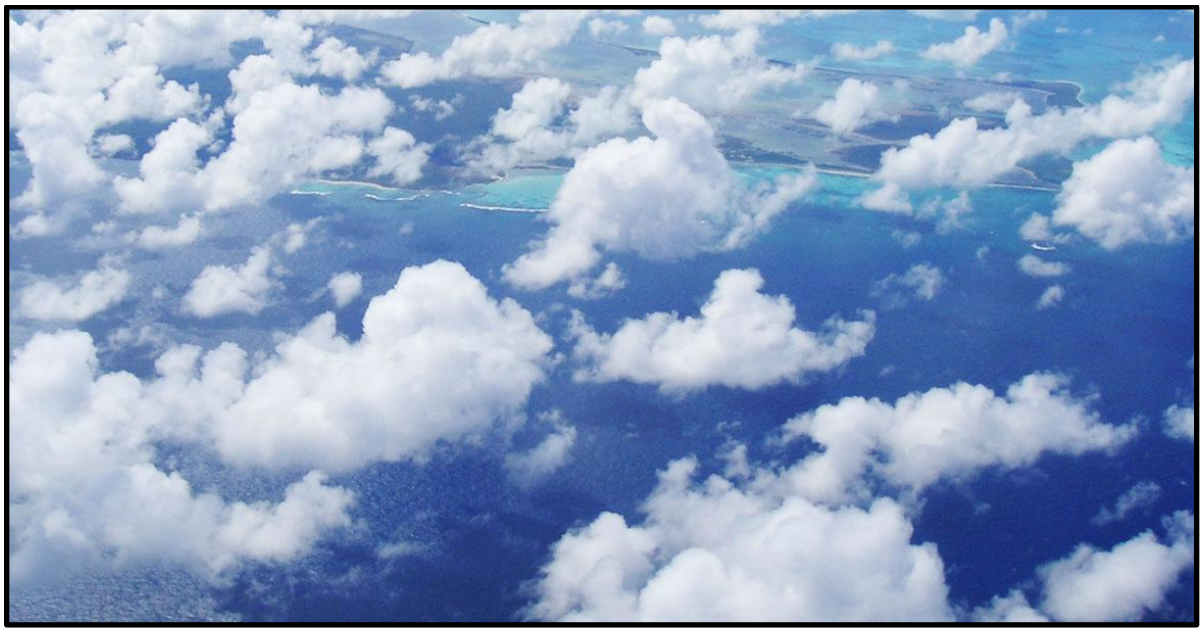

Figure 13. An aerial photograph of a typical trade wind cumulus cloud field observed in the Western Caribbean during the Rain in Cumulus over Ocean (RICO) field program. Apparent is the wide range of cloud depths and horizontal extents. (Image courtesy of B. Stevens).

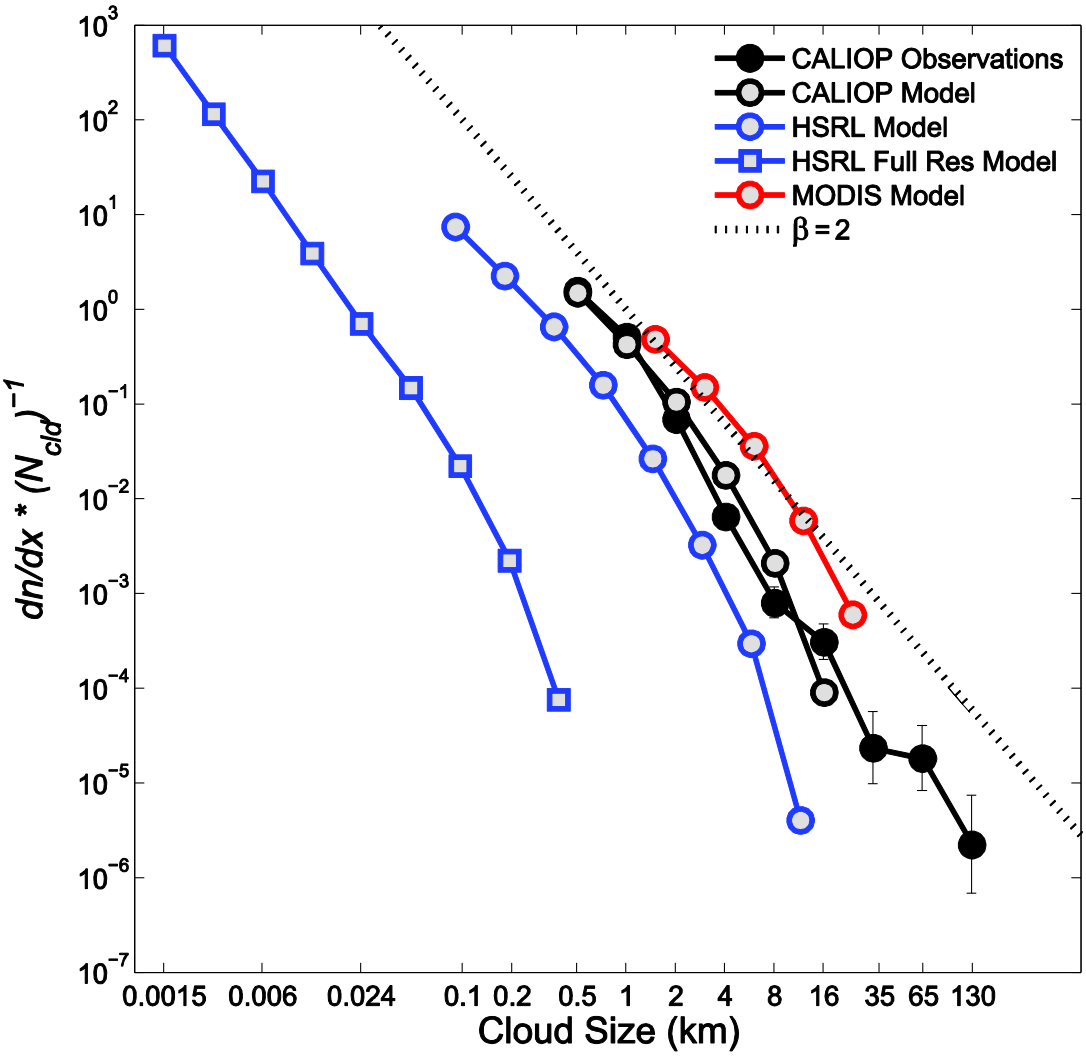

Figure 14. Two years of CALIOP tropical Pacific trade wind region observations (black dots) ± 95% confidence intervals from bootstrap method [*Efron and Gong*, 1983], and cascade model output simulating this cloud regime, sampled with CALIOP FOV (black circles), MODIS FOV (red circles), HSRL FOV (blue circles), and HSRL Full Res i.e., highest resolution sampling of model output (blue squares). Size bins are logarithmically spaced and ordinate axis is normalized frequency. β = 2 line (dashed line) shown for reference. Cascade model output from 100 runs with H = 0.015 and p = 0.05. Abscissa values are cloud length bin centers.

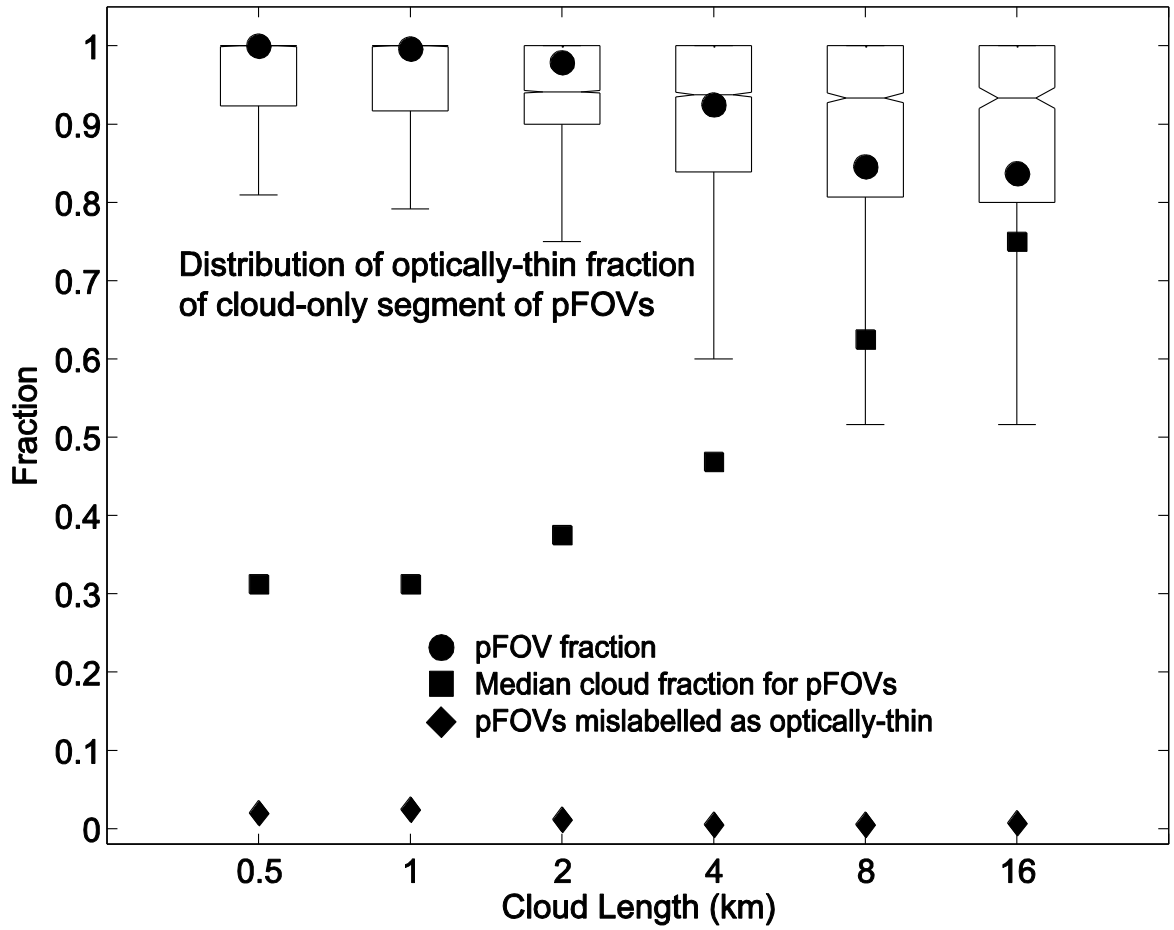

Figure 15. Cloudy FOVs and partially cloud-filled FOVs (pFOVs) metrics binned by cloud length, as described by model simulated optical depth (τ) values, sampled at CALIOP FOV resolution. Displayed for each cloud length-bin is the fraction of all cloud FOVs that are less than 100% cloudy, i.e., pFOV (filled circles); the median cloud fraction for pFOVs (filled squares); the fraction of optically-thin pFOVs incorrectly classified as optically-thin, i.e., a FOV with mean τ less than or equal to 3 and mean τ of the cloudy-only segment greater than 3 (filled diamonds); the distribution of the optically-thin fraction of the cloud segment within a pFOV, where the box notch indicates that median fraction, upper and lower lines are the upper and lower quartile values, and whiskers are 1.5 x interquartile range. Cascade model output from 100 runs with H = 0.015 and p = 0.05.